2016

Dynamic Modeling of Autorotation for Simultaneous Lift and Wind Energy Extraction

Sadaf Mackertich
University of Central Florida

DYNAMIC MODELING OF AUTOROTATION FOR SIMULTANEOUS LIFT AND WIND ENERGY EXTRACTION

by

SADAF MACKERTICH
B.S. Rochester Institute of Technology, 2012

A thesis submitted in partial fulfilment of the requirements
for the degree of Master of Science
in the Department of Mechanical and Aerospace Engineering
in the College of Engineering and Computer Science
at the University of Central Florida
Orlando, Florida

Spring Term
2016

Major Professor: Tuhin Das

ABSTRACT

The goal of this thesis is to develop a multi-body dynamics model of autorotation with the objective of studying its application in energy harvesting. A rotor undergoing autorotation is termed an Autogyro. In the autorotation mode, the rotor is unpowered and its interaction with the wind causes an upward thrust force. The theory of an autorotating rotorcraft was originally studied for achieving safe flight at low speeds and later used for safe descent of helicopters under engine failure. The concept can potentially be used as a means to collect high-altitude wind energy. Autorotation is inherently a dynamic process and requires detailed models for characterization.

Existing models of autorotation assume steady operating conditions with constant angular velocity of the rotor. The models provide spatially averaged aerodynamic forces and torques. While these steady-autorotation models are used to create a basis for the dynamic model developed in this thesis, the latter uses a Lagrangian formulation to determine the equations of motion. The aerodynamic effects on the blades that produce thrust forces, in-plane torques, and out-of-plane torques, are modeled as non-conservative forces within the Lagrangian framework. To incorporate the instantaneous aerodynamic forces, the above-mentioned spatial averaging is removed. The resulting model is causal and consists of a system of differential equations. To investigate the dynamics under energy-harvesting operation, an additional in-plane regenerative torque is added to simulate the effect of a generator. The aerodynamic effects of this regenerative braking is incorporated into the model. In addition, the dynamic model relaxes assumptions of small flapping angles, and the periodic flapping behavior of the blades are naturally generated by the dynamics instead of assuming Fourier expansions. The dynamic model enables the study of transients due to change in operating conditions or external influences such as wind speeds. It also helps gain insight

into force and torque fluctuations.

Model verification is conducted to ensure that the dynamic model produces similar steady-operating conditions as those reported in prior works. In addition, the behavior of autorotation under energy harvesting is evaluated. The thesis also explores the viability of achieving sufficient lift while extracting energy from prevailing winds. A range of regenerative torques are applied to determine the optimal energy state. Finally, a complete high-altitude energy harvesting system is modeled by incorporating a tether utilizing a catenary model. Overall, the thesis lends support to the hypothesis that a tethered autogyro can support its weight while harvesting energy from strong wind-fields, when augmented with appropriate control systems.

To my mom Shanzida, my dad Shahidullah, my sister Shadia, and my brother-in-law Keniel who have supported me through my decision to pursue higher education. To my friends Dan and Chris who have brought me much laughter and happiness. And finally, to my niece and nephew Keniel Veron Lee Jr. and Sadira Suhani Lee who have shown me that one can never be too silly.

ACKNOWLEDGMENTS

First and foremost I would like to acknowledge my advisor Dr. Tuhin K. Das who has mentally and financially supported me through this endeavor. Without his help this research would not be where it is. I would also like to thank my committee members Yunjun Xu and Faissal Moslehy for their assistance and feedback on this research.

The dream of flight has been with mankind since before the days of Leonardo da Vinci. To be able to soar among the birds have been a difficult journey. A journey that has taken hundreds of years and amazing discoveries in mathematics, aerodynamics, and mechanics to achieve. My work would be meaningless without these achievements. I acknowledge the genius of my predecessors as I stand on their shoulders to see further.

TABLE OF CONTENTS

LIST OF FIGURES

LIST OF TABLES

NOMENCLATURE

a Slope of lift curve for infinite aspect ratio

b Number of blades

c Blade chord

t_h Airfoil thickness

W_d Total weight

I_1 Blade moment of inertia about flapping hinge

H Longitudinal force

C_T Rotor thrust coefficient

C_{L_r} Rotor lift coefficient

C_{D_r} Rotor drag coefficient

Q_e Aerodynamic Torque

Q_h Shaft-torque required for hover

R Blade radius

B Blade radius fraction less tip losses

T Thrust force

D Drag force

V Velocity of aircraft/wind

V_η Required wind speed for steady autorotation

V_c Climb Velocity

V_d Descent Velocity

D Effective drag force

H Longitudinal force

L Effective lift force

θ_0 Blade pitch angle at root

θ_l Blade pitch slope

α Angle of incidence

β Angle of blade with respect to rotor disk plane

φ Angle of oncoming wind at blade element

a_0, a_1, b_1, a_2, b_2 Fourier series parameters of flapping

α_r Angle of incidence at blade element

μ Tip speed ratio

ν Induced axial velocity

ν_h Induced axial velocity during hover

λ Axial flow ratio

ρ Density of air

σ Blade solidity

ψ Angular position of blade

Ω Angular velocity about shaft

M_W Flapping moment from blade weight

M_T Flapping moment from thrust

r_H Hub radius

r_{a_i} Radius vector from center of rotation to center of mass of blade

m_b Mass of blade

m_a Mass of autogyro

m_t Mass of tether

g Acceleration due to gravity

δ Air drag constant

x_e, y_e Equilibrium point along the x-y axis

R Reaction force on tether from ground

F_c Reaction force on autogyro from tether

l_t Length of tether

η_0 Angle of tether with respect to ground

η_l Angle of tether with respect to gravity vector

U_T Velocity perpendicular to blade and center of rotation

U_P Velocity parallel to center of rotation

U_R Velocity perpendicular to U_T and U_P

LTA Lighter than air

AWE Airborne Wind Energy

CHAPTER 1: INTRODUCTION

1.1 Motivation

With depleting resources and an unsustainable growth of energy demands, researchers look towards new methods to supplement the world energy demands. High altitude wind data shows there is constant and abundant levels of kinetic energy available, that is not restricted by geographical locations. Studies done of wind power at altitudes of 7-16km show an abundance of power at least an order of magnitude higher than global demand [7, 8]. Data mining efforts, shown in Fig.1.1, prove that widespread, consistent wind patterns exist at high altitudes with maximum wind speeds occurring around 10km. The three locations Atlanta (GA), Buffalo (NY), and Great Falls (MT) in Fig.1.1 were chosen to span a wide range of surface wind speeds. For instance, Atlanta belongs to Class 1 in Fig.1.2(a), Great Falls belongs to Class 3-4, and Buffalo belongs to Class 4-5. The following observations can be made: **(1)** In spite of significant variability in surface wind speeds, the wind speed variation with altitude and the magnitudes of the average maximum wind speeds are similar at all three locations; **(2)** Average wind speeds increase steadily with altitude, up to ≈ 10 km.

Wind power at lower altitudes has different spatial characteristics. A report done by the National Renewable Energy Laboratory (NREL) [9] shows wide variability of wind distributions and states that wind energy extraction is only viable for wind power classes of 3 and above, Fig.1.2. On the other hand, high altitudes show consistency throughout regions that can be attributed to the existence of jet streams and global climate phenomena. Due to these jet streams total available wind energy can be roughly 100 times the global energy demand [7].

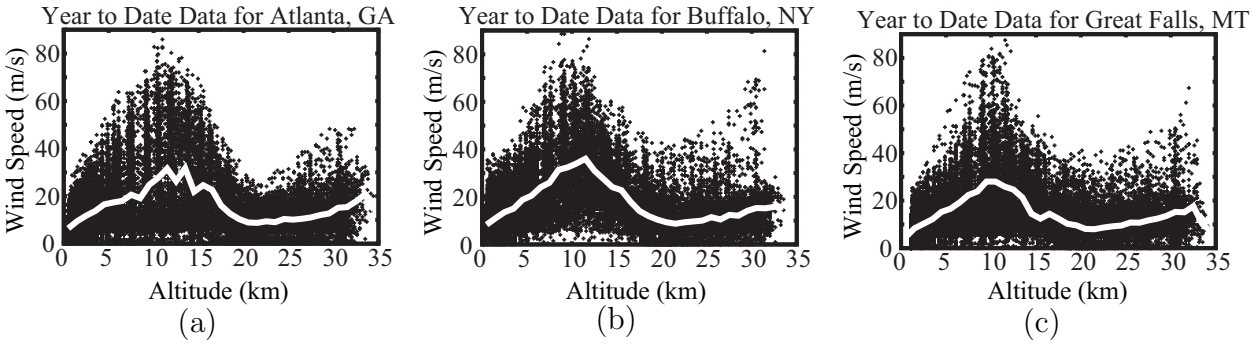

Figure 1.1: Wind velocities at different cities. White line represents average (a) Wind speeds at Atlanta, GA (b) Wind speeds at Buffalo, NY (c) Wind speeds at Great Falls, MT

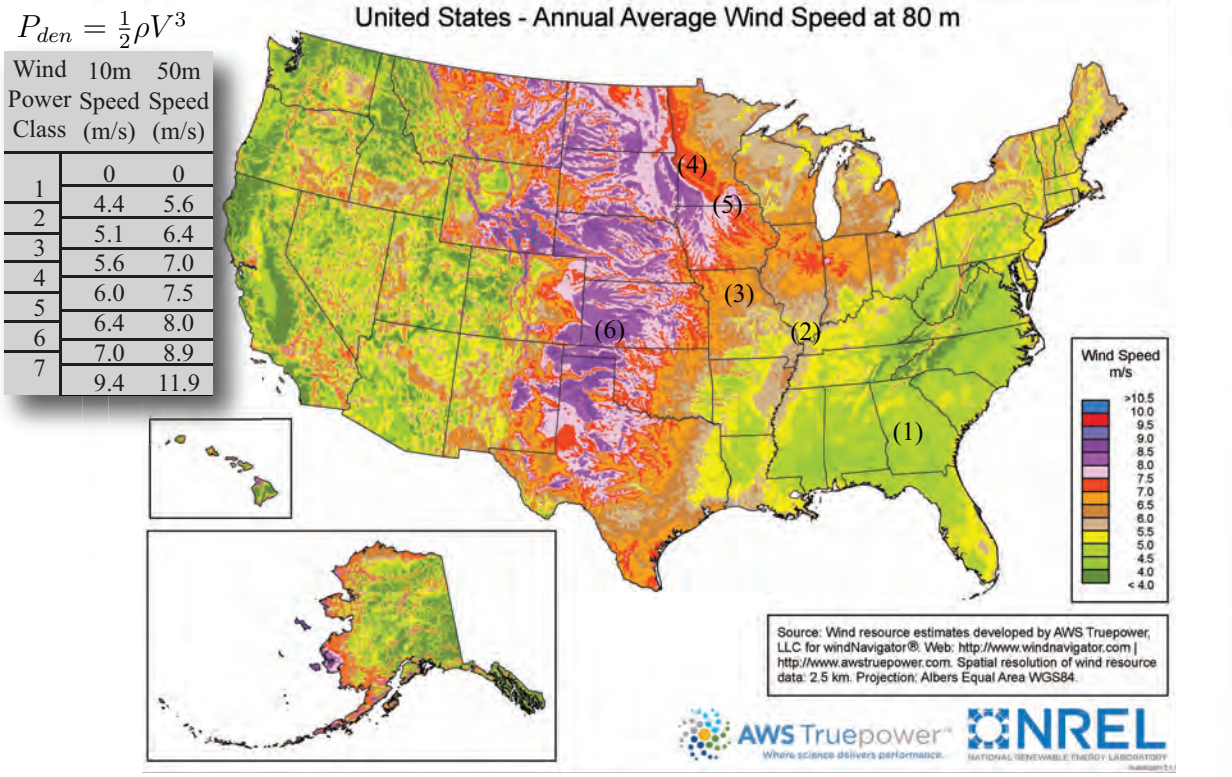

Wind Power Class	10m Speed (m/s)	50m Speed (m/s)
1	0	0
2	4.4	5.6
3	5.1	6.4
4	5.6	7.0
5	6.0	7.5
6	6.4	8.0
7	7.0	8.9
	9.4	11.9

Figure 1.2: (a) Average annual surface wind energy distribution map [1]

To quantify the overall amount of power a thorough analysis of Buffalo, NY is performed. It is important to consider the variation of density with altitude, therefore, wind power density at different altitudes can be estimated using the relation: $P_{den} = 0.5\,\rho V^3$, where ρ and V are the density and the velocity of wind, respectively. Due to similarities in velocity profiles across locations, the variation of wind power with altitude was investigated using the data for Buffalo, NY. The results are shown in Fig.1.3. Figure 1.3(a) shows the probability distribution of wind speed above a certain value at different altitudes and Fig.1.3(b) plots the wind power from the raw data in Fig.1.2(b). Note that although the wind speed can be significant at altitudes of 15km and higher, the wind power available diminishes sharply due to atmospheric rarefaction (at 10km, $\rho \approx 0.41\text{kg/m}^3$; at sea level $\rho \approx 1.22\text{kg/m}^3$). Figure 1.3(c) shows a comparison of probability distributions of wind power densities at altitudes in the range $1 - 12$ km. Clearly the abundance of wind power is enormous but adds the challenge of achieving lift and collecting energy simultaneously.

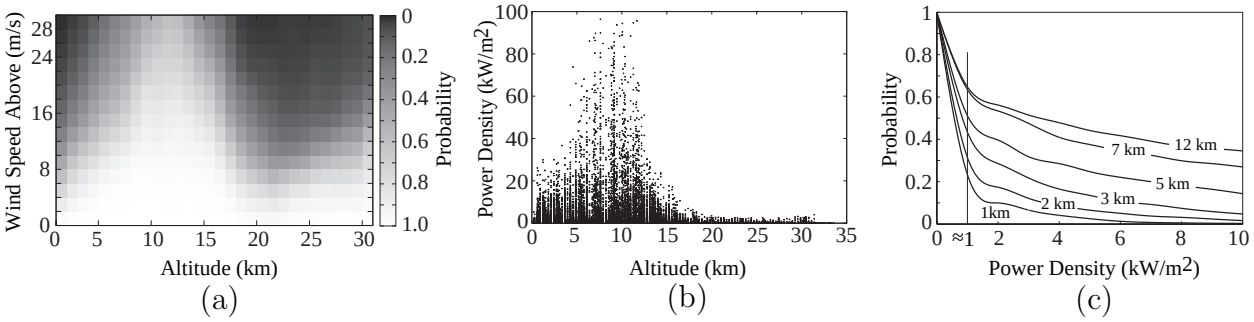

Figure 1.3: High-altitude wind power estimation for Buffalo (NY) shows a trend that can be observed across different locations in the US.

1.2 Autorotation

A number of designs have been proposed for AWE extraction. A review of these existing designs can be found in [10]. The review confirms that current research has exclusively con-

sidered tethered AWE devices for relatively low altitudes, $\leq$ 1km. However, to substantially benefit from high energy densities, one must extend the altitude of operation, preferably to $\geq$ 5km, where an important challenge is posed by the tether. Without a tether, the AWE device would drift in the wind. But in its presence, the tether itself would significantly add to the total weight. Mechanical transmission of power through tether tension is also impractical for high altitudes, due to excessive lag. Moreover, the tether remains a deterrent on the grounds of aviation safety. Research done on hot air balloons, [11], has indicated that although a lighter-than-air (LTA) device such as hot air/helium balloon with retrofitted wind turbine(s) may seem pragmatic for simultaneous lift and power generation, its main drawback is the lack of maneuverability. The authors in [12, 13] also investigated wind energy harvesting using tethered airfoils where the tether tension is used to mechanically transmit power to the ground. It was concluded from these studies that while a tethered airfoil may be suitable as an AWE device for low altitudes, there are challenges of harvesting energy from high altitudes. In comparison, autorotation appears to have a number of advantages.

The principle of *autorotation* can be considered as a generalization of the helicopter. While a helicopter generates vertical thrust by accelerating air in the downward direction, autorotation is achieved by placing a freely turning rotor inclined to a wind field. The result is a rotation and an upward thrust, as shown in Fig.1.4. A rotor undergoing autorotation is termed an *autogyro*. Traditionally, autorotation has been investigated to build gyrocopters [14, 15], or in the context of safe landing of helicopters in case of engine failure, [16], but has not been investigated for wind energy extraction. The blades of an autogyro are free to spin about their common axis, and each blade is additionally free to rotate (flap) about a hinge at its root normal to the spin axis, Fig.1.4(b). The rationale behind investigating the autogyro mechanism is the following: If a rotor-craft can switch between powered flight and autorotation modes, then it can selectively harvest energy when a strong wind field is

present.

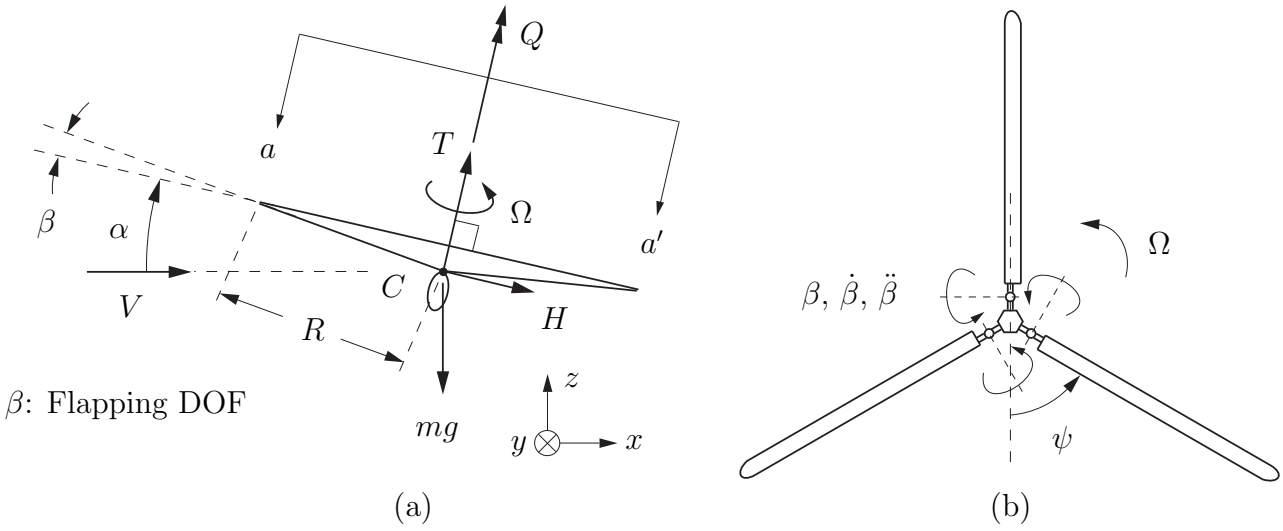

Figure 1.4: (a) Forces on an Autogyro (b) View from plane $a - a'$

The theory of autorotation can be traced back to the work published in [17]. BEM (Blade Element Momentum) approach was used to model aerodynamic forces, [18]. Several works followed [17] to further improve the theoretical basis of autorotation. In particular, in [6], blades with varying pitch were considered to validate against experimental data from Pitcairn-Cierva Autogyro [14, 4, 15]. The work also incorporated a detailed analysis of the forces in the retreating half (see Fig.3.1(a), (d)), where the blade velocities are reversed. A variant of the autogyro, known as the gyroplane, was studied in [19]. A gyroplane has an even number of blades; the opposite blades are rigidly connected and are allowed to *feather*, *i.e.*, freely rotate about their span axis. Although the gyroplane is structurally different from the autogyro, both have additional DOFs compared to wind turbines and results in [19] indicate that they have similar overall lift-coefficients and lift/drag ratios. Other extensions include modeling the effect of twisting of blades in [20], and refinement of the analysis of the retreating half for larger angles of attack and higher speeds in [21].

1.3 Thesis Organization

This thesis represents an extension of the work done in [22] by employing refined theories of autorotation presented in [6] and utilizing Lagrangian mechanics with modern numerical tools to create a dynamic model. Chapter 2 is split into two sections: **1)** airborne wind energy systems are reviewed and **2)** a review of autorotation and the autogyro is provided. Chapter 3 reviews the work of [6] and provides a basis for autorotation modeling. The model is verified with [6] and used to study the effects of flapping on thrust. Chapter 4 develops the dynamic model of autorotation for energy harvesting. Verification is done by comparing steady-state solutions with [6]. Chapter 5 studies the feasibility of extracting energy while maintaining sufficient lift. An analysis is performed to determine the behavior of the system with the introduction of a generator load utilizing the two theories presented in this paper. Then the maximum generator load that can be applied for optimal energy extraction is determined. Chapter 6 examines a tethered autogyro employing a catenary model. The model allows for determining equilibrium positions of the autogyro while extracting energy and sustaining the added weight of the tether. Finally, chapter 7 reviews the overall outcome of this research and discusses future work.

CHAPTER 2: LITERATURE REVIEW

Research into Airborne Wind Energy Systems (AWES) started in the mid seventies but within the last decade it has attracted further research. Due to an increase in global warming and a depletion of natural resources, alternative energy solutions are seriously being considered. Leaders of the European Union have placed an objective to reduce greenhouse gas emissions by a minimum of 80% below 1990 levels by 2050 [23]. In the U.S., the Department of Energy has proposed offloading 20% of energy demand onto wind by 2030 [24]. Total power production in the US is a little over 1 TW per year. According to [25], the United States approximately consumes 3,832 TWh of energy per year. The current production of wind energy, according to [2], is approximately 65,879 MWh, Fig.2.1. Therefore, wind energy accounts for only 6.6% of U.S. total energy production. Calculated available wind power at high altitude ranges from 400 TW to 1800 TW [26], which far exceeds global demand. However, disagreements exist on how much power can be extracted without causing significant effect on the climate. The authors in [26] and [27] disagree on the maximum power that can be extracted. While [26] claim that 18 TW of power can be safely produced, the authors in [27] show a different outcome where only 7.5 TW can be gathered and going beyond that may have serious repercussions such as global climate change.

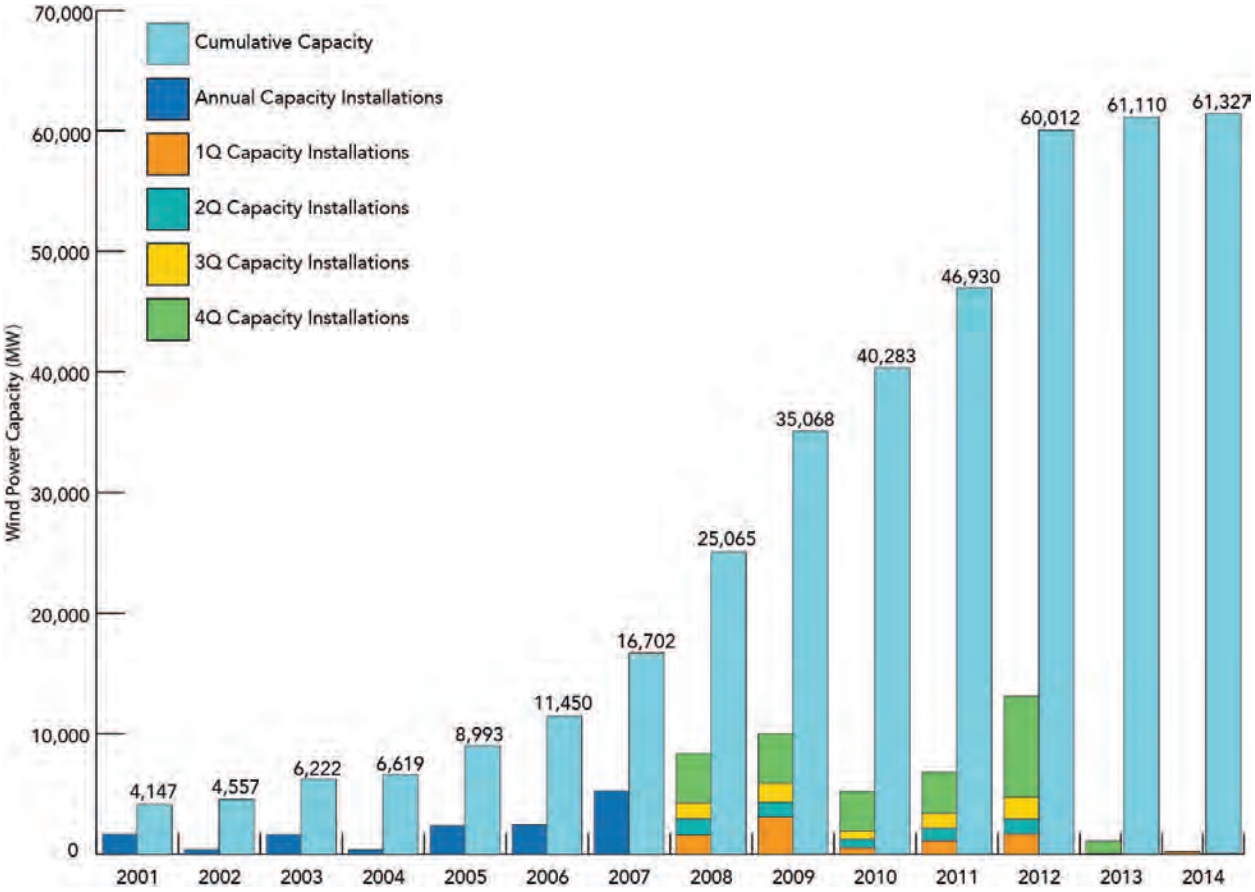

Figure 2.1: U.S. Wind Power Capacity. Reproduced from [2]

Many variations of AWE's have already been suggested and researched. In section 2.1 a review of these systems are provided. A more rigorous review of AWES and companies pursuing them are presented in [3]. Although Skywindpower [28] built prototypes based on autorotation, the theoretical understanding of autorotation under energy harvesting were not explored. This research looks further into energy extraction via autorotation and attempts to provide a detailed model characterizing the system.

2.1 Current State of AWES

Airborne wind energy systems can be broken down into two designs shown in Fig.2.2. The first being ground based energy extraction where a device such as a kite provides the necessary force to rotate/move a generator. The second design houses a generator on-board the airborne device. Generally, most designs employ a tether to either use as a mechanism to transmit force or electricity. The implications of each design are review in the following sections.

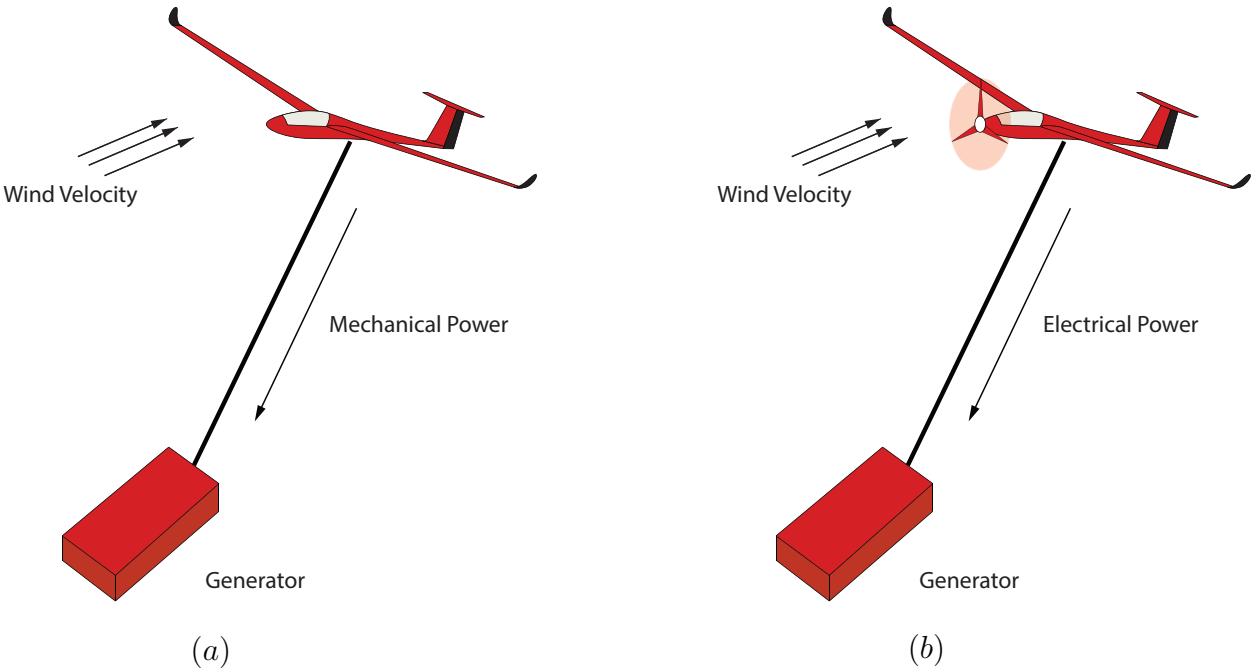

Figure 2.2: (a) Ground based extraction (b) Airborne extraction. Reproduced from [3]

2.1.1 Ground Based Energy Extraction

Ground based energy extraction relies on a kite or airfoil to turn a generator on the ground. By placing the generator on the ground is a significant weight weight reduction occurs.

Ground based generator designs with a moving base and a fixed base have been proposed. The systems use a two-phase cycle composed of a generation phase and recovery phase Fig.2.3.

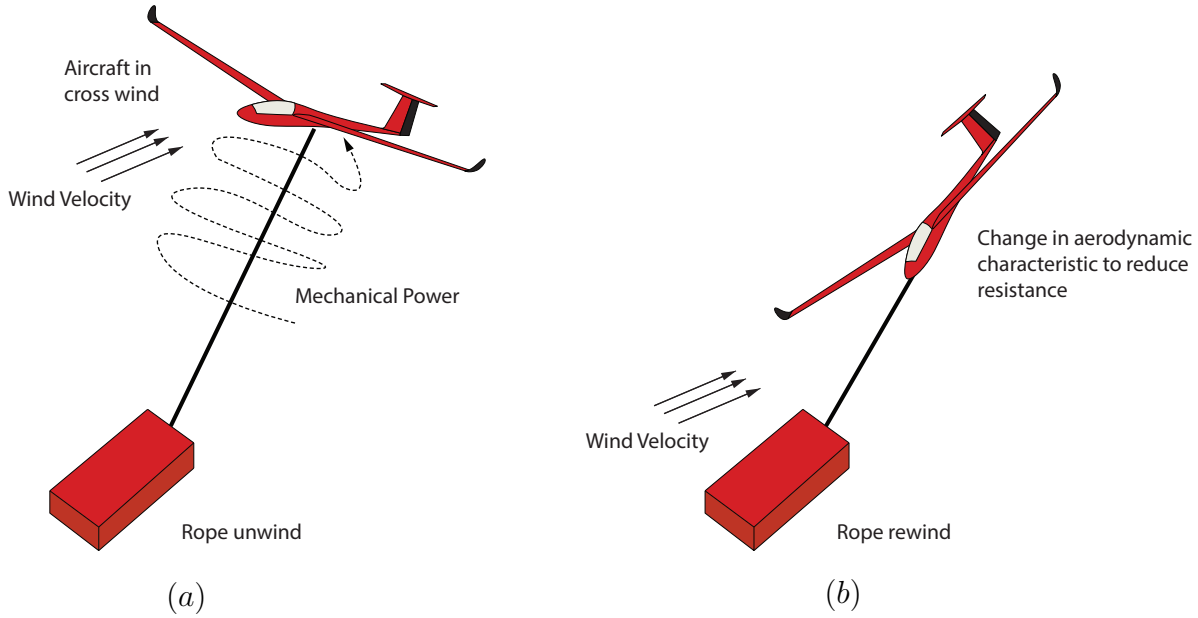

Figure 2.3: (a) Generation Phase (b) Recovery Phase. Reproduced from [3]

The generation phase occurs when the airfoil or kite experiences a crosswind which provides the traction required to turn or move the base depending on the design. For the recovery phase the tether is drawn back and the angle-of-attack or the effective resistance of the airfoil is lowered in order to get net-positive energy. Control of these kites/airfoils are performed through ropes or actuators as shown in Fig.2.4.

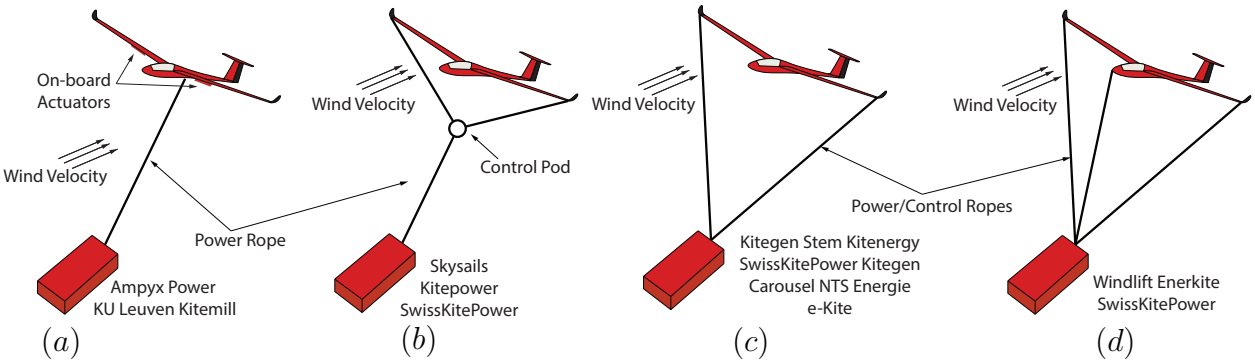

Figure 2.4: Examples of tether control systems. Reproduced from [3]

In [29, 30, 31, 32] the authors have studied these kite based designs and also proposed a new Laddermill, multi-kite, type device. However, the issue with these devices is they cannot be used for high altitudes $\geq 5km$, which is the focus of this paper, because of the increased lag experienced from a longer tether. In addition, for stationary ground generators the two phase cycle creates long discontinuous power times requiring batteries or capacitors for storing energy. A way to alleviate this issue is by introducing a moving base. The moving base allows for continuous power production as shown in Fig.2.5.

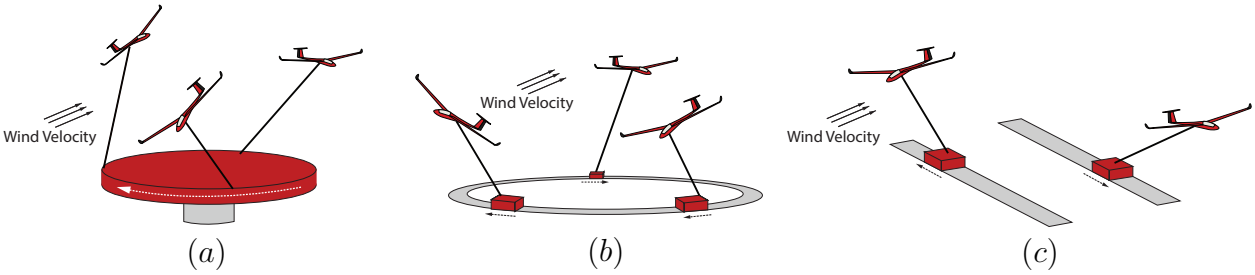

Figure 2.5: Moving base designs. Reproduced from [3]

2.1.2 On-board Energy Extraction

Another design for AWES involves extracting wind energy on-board the device and sending it down via a tether. Most designs use a turbine to turn a generator in order to produce power with the exception of a proposed design that would take advantage of the Magnus effect [33, 34] . The differences in each design lie in how lift is achieved, shown in Fig.2.6. In Fig.2.6a and 2.6, both devices use a dual lift system where initially the lift is carried out by turbines similar to a quad-rotor until the system has reached its working altitude at which point the device acts as a regular airfoil achieving lift from wind flow [35, 36, 37]. Makani Power Inc., recently acquired by Google, is focused on building a 600kW eight turbine prototype [38]. A second popular design currently being pursued by Altaeros Energies is a lighter than air aerostat shown in Fig.2.6(c). The device itself houses a generator on-board but simplifies the difficulty of lift by making the system lighter than air thereby achieving lift via buoyancy. The final design initially pursued by SkywindPower [28] is a quadrotor design that relies on autorotation.

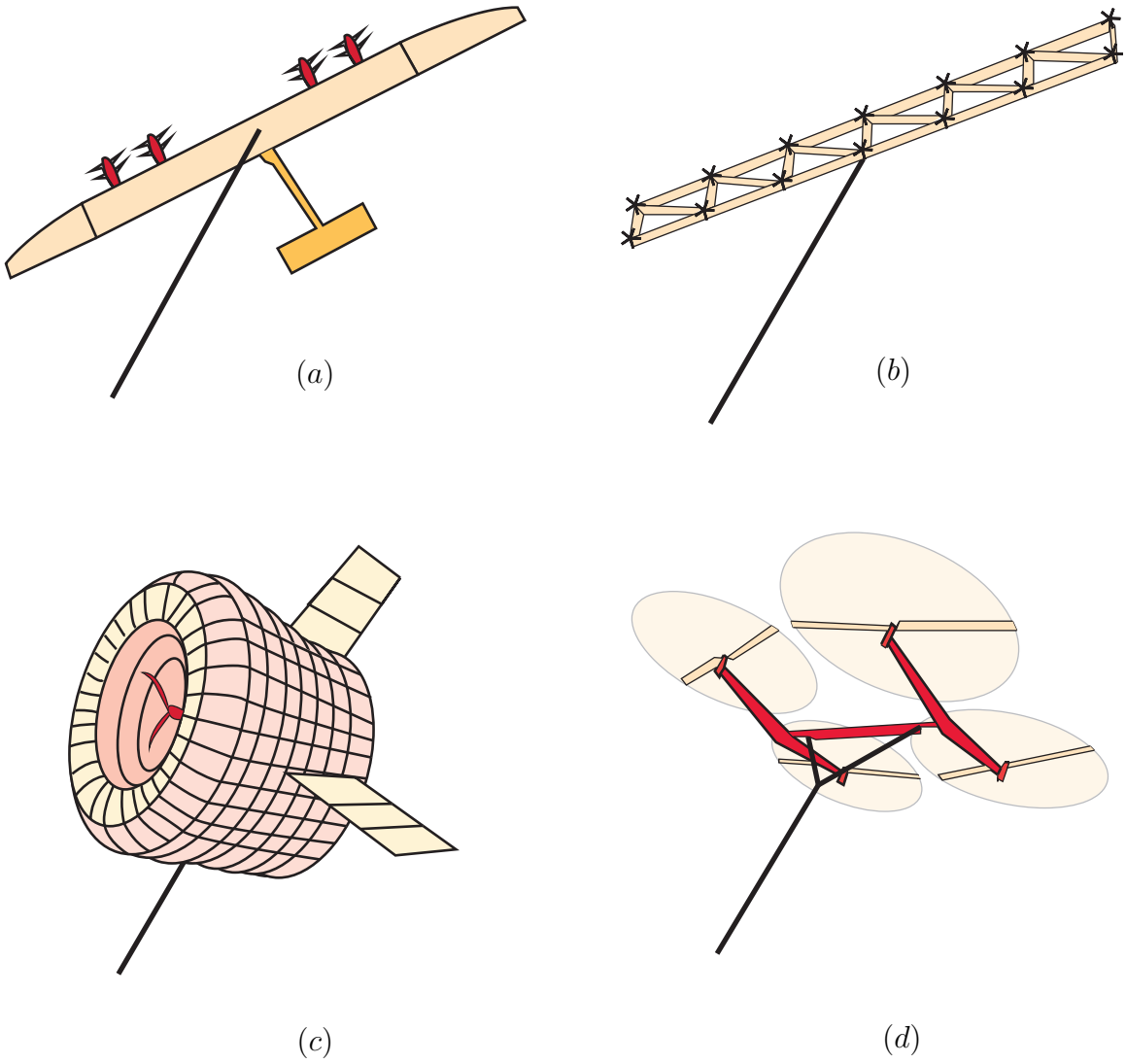

Figure 2.6: (a) Aerofoil (b) Laddermill (c) Balloon (d) Autorotation. Reproduced from [3]

Autorotation relies on wind flow through a rotor to generate lift. Autorotation has been shown by Juan de la Cierva to be an effective and simplistic way to generate lift through a spinning rotor. Even though crosswind has been shown to be more effective in drawing more power the autogiro, as de la Cierva coined it, is more easily controlled and does not rely on high tether tension, which may not be feasible at very high altitudes. Unlike SkywindPower that looked at altitudes around $5km$ this thesis analyzes the possibility of altitudes up to

$10km$. This adds more weight and complexity due to the dynamics of the tether. Therefore, it is important to consider the literature in order to characterize and determine the feasibility of utilizing autorotation for energy harvesting.

2.2 Autorotation and Autogyro Dynamics

Although the autogyro and helicopter may appear similar the two are inherently different. In fact, a lot of autorotation work led to the development of helicopters. Helicopters rely on airflow down through the rotor where as autorotation depends on air flow upwards through the rotor, Fig.2.7. Leishman [4] provides an in-dept look at the technical history and development of the autogyro. In addition, Leishman shows that research on autogyros virtually halted after helicopters came into development. Only recently has the work on autogyros and gyroplanes resurfaced.

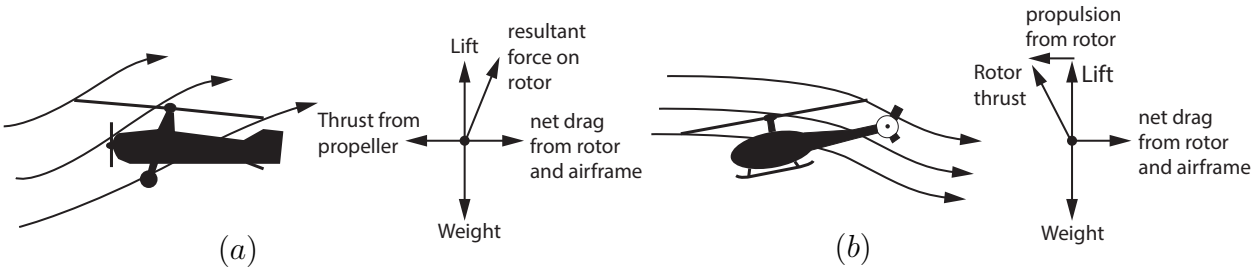

Figure 2.7: (a) Autogyro: Inflow upwards through the rotor disk (b) Helicopter: Inflow downward through the rotor disk. Reproduced from [4]

A considerable amount of theoretical and experimental work was completed by Glauert, Wheatley, Lock and Bailey around the 1930's [17, 39, 40, 6, 19, 41, 42]. Juan de la Cierva would be the first to build and test the autogyro and pave the way for the future of gyroplanes [43, 44, 45, 46]. Autorotation can be thought of as a self-sustained rotation of a rotor with net shaft torque $Q = 0$. This implies the energy required to turn the rotor must come from

the relative airstream. The rotor torque ratio Q/Q_h where Q_h is the torque required to hover can be defined as

$$\frac{Q}{Q_h} = \frac{V_c}{v_h} + \frac{v_i}{v_h} \tag{2.1}$$

where V_c is the climb velocity, ν_i is the induced velocity, and ν_h is the induced velocity at hover. Early experimental studies show that classical momentum theory does not apply for the region $-2 \leq \frac{V_c}{V_h} \leq 0$ [5], shown in Fig.2.8. Thus, autorotation cannot directly rely on momentum theory as it consistently lies in this region. Therefore, [17] developed an initial model that used a combination of momentum theory, blade element theory, and an empirical formulation for induced velocity. This model was further improved through experimental data presented in [19]. A thorough review of the autorotation model from [6] is completed in section 3.

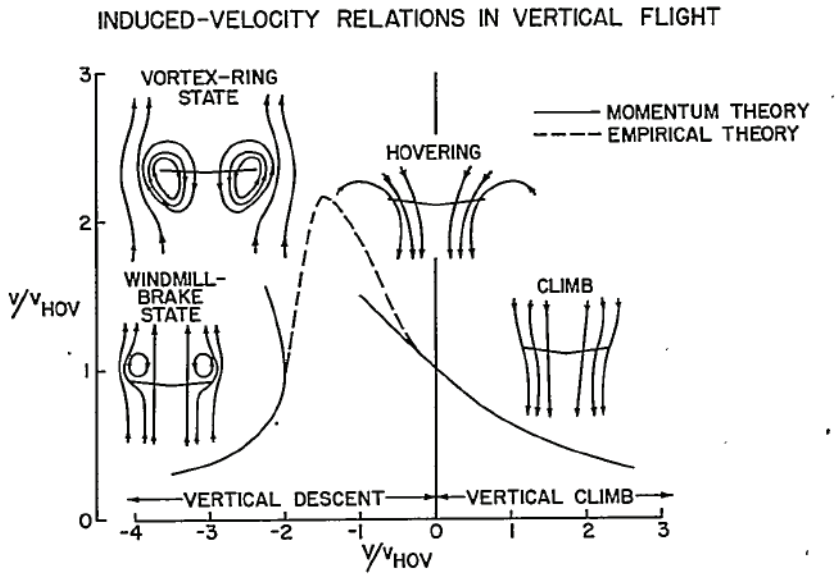

Figure 2.8: Momentum Theory Curve. Reproduced from [5]

A significant sticking point before the autogyro could sustain level flight is the issue of asymmetric lift. During normal hover, the relative velocities in the forward and reverse half

regions, shown in Fig.2.9a, are the same. However, when the aircraft moves forward the relative velocities in the forward and reverse half regions differ causing unequal lift, Fig.2.9b. To resolve this issue Juan de la Cierva introduced a hinge that would allow each blade to flap as it rotated. This effectively balances out the forces by reducing lift in the forward half and increasing lift in the reverse half as the blade rotates through the two regions. Balancing occurs because as a blade experiences higher wind velocities the blade rises causing a decrease in lift. The opposite occurs in the reverse flow region. As relative wind velocities decrease, the blade falls thereby increasing dynamic pressure and lift. Additionally, if the rotor disk is turning counterclockwise the disk has a tendency to tilt laterally to the right. This phenomenon occurs because as the blade crosses $\psi = 0^\circ$ it has a higher lift vector than at $\psi = 180^\circ$ causing the rotor disk to tilt. However, with the introduction of blade flapping Coriolis forces come into play. Since angular momentum must be conserved, as the blade flaps the radius of gyration changes which causes a stress to be introduced at the blade root. To prevent catastrophic failure of the blade a set of lead-lag hinges were added to balance out the in-plane centrifugal forces that arise from adding the flapping degree-of-freedom.

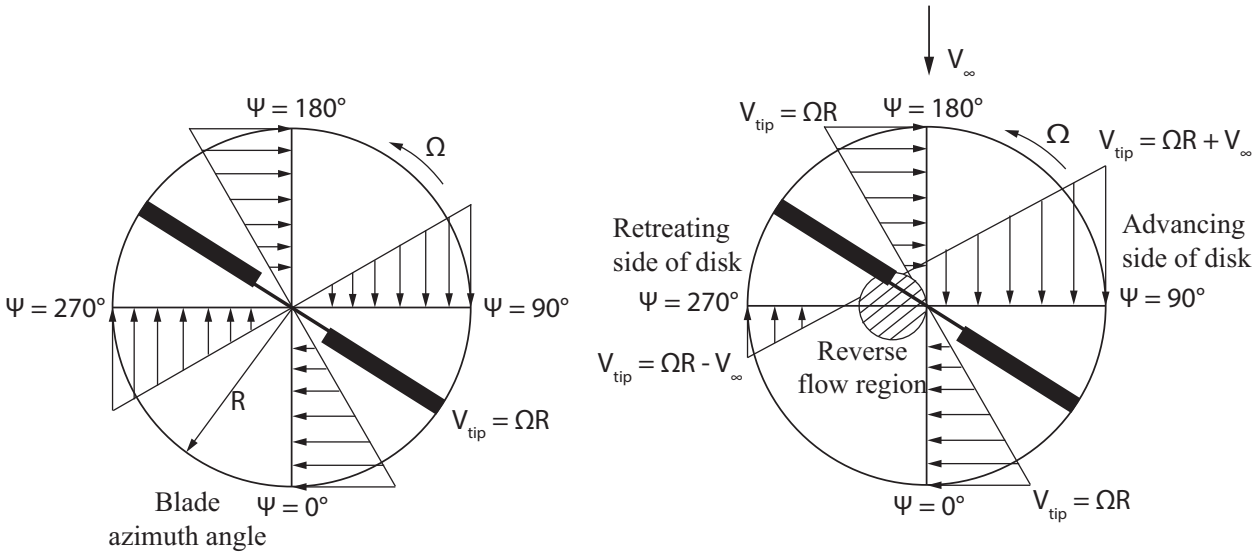

Figure 2.9: Asymmetric Lift Dilemma. Adapted from [4]

As a rotor goes through autorotation it experiences variable wind speed along the blade-span affecting aerodynamic blade torque. The distribution of blade torque is shown in Fig.2.10. Since the inward section of the blade experiences higher angles-of-attack, the driving force is higher than that of drag, causing a net-positive torque. Towards the end of the blade-span, the higher relative velocities decrease the angle-of-attack causing a decrease in the driving force and an increase of the drag force, Fig.2.10. This effectively causes a net-negative torque slowing down the blade. Between these two regions lies the point of ideal autorotation where the torque $Q = 0$. As a blade spins faster, the neutral autorotation point moves inward toward the blade-root.

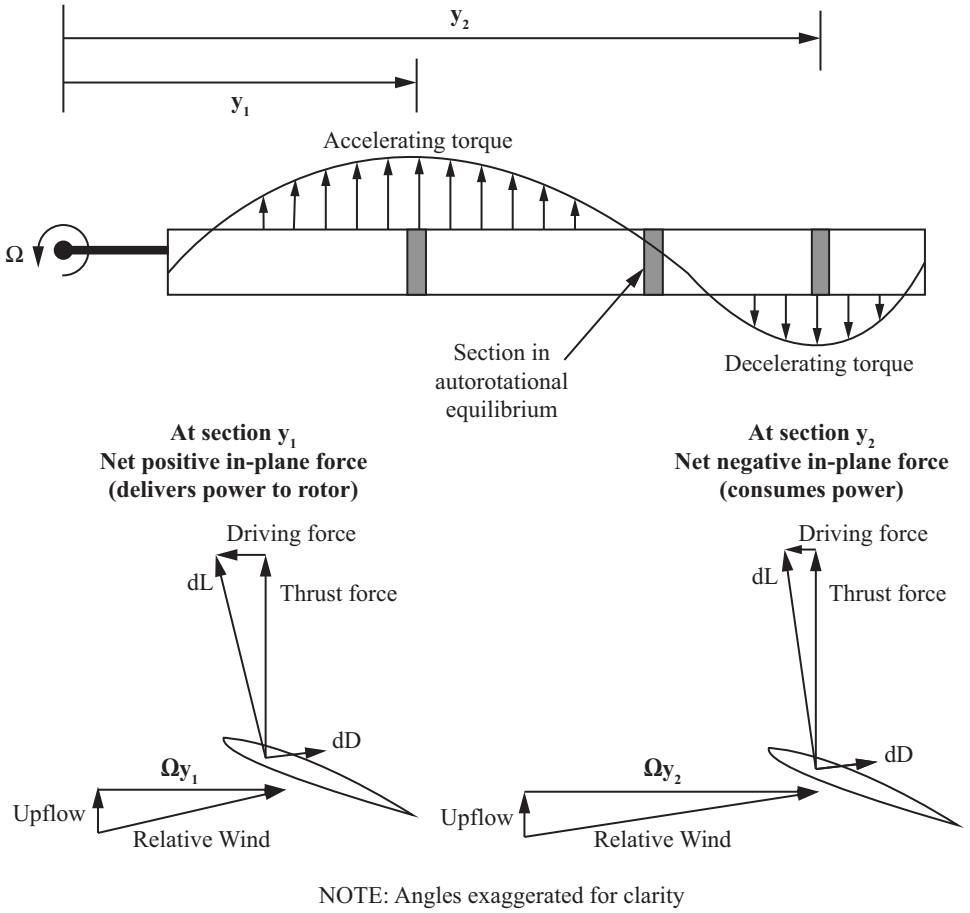

Figure 2.10: Blade torque distribution in steady-state autorotation. Reproduced from [4]

Another challenge in achieving safe flight in rotorcrafts, is limiting the sectional blade angle-of-attack. The angle-of-attack, unlike an airplane, changes along the blade length. Since rotation is purely determined by aerodynamic forces, the angle-of-attack must remain within certain boundaries to maintain stable flight. Angle-of-attack α is defined as $\alpha = \varphi + \theta$ where θ is the blade pitch and φ is the inflow ratio defined as

$$\varphi = \frac{\text{Upflow velocity}}{\text{In-plane velocity}} = \arctan\left(\frac{|V_c + \nu_i|}{\Omega r}\right) \tag{2.2}$$

Wimperis [47] developed a graphical method to show these critical angles, Fig.2.11. The diagram in 2.11 shows the drag-lift ratio C_d/C_l vs the angle-of-attack. Points A,B, and C are on the line of ideal autorotation or

$$C_d - \varphi C_l = 0 \quad \rightarrow \quad \frac{C_d}{C_l} = \varphi = \alpha - \theta \tag{2.3}$$

Any points behind this line causes accelerating torque where anything past that line consumes energy thereby causing decelerating torque. At point D a maximum angle-of-attack is reached where anything past this point causes rotor rpm to quickly decay [4].

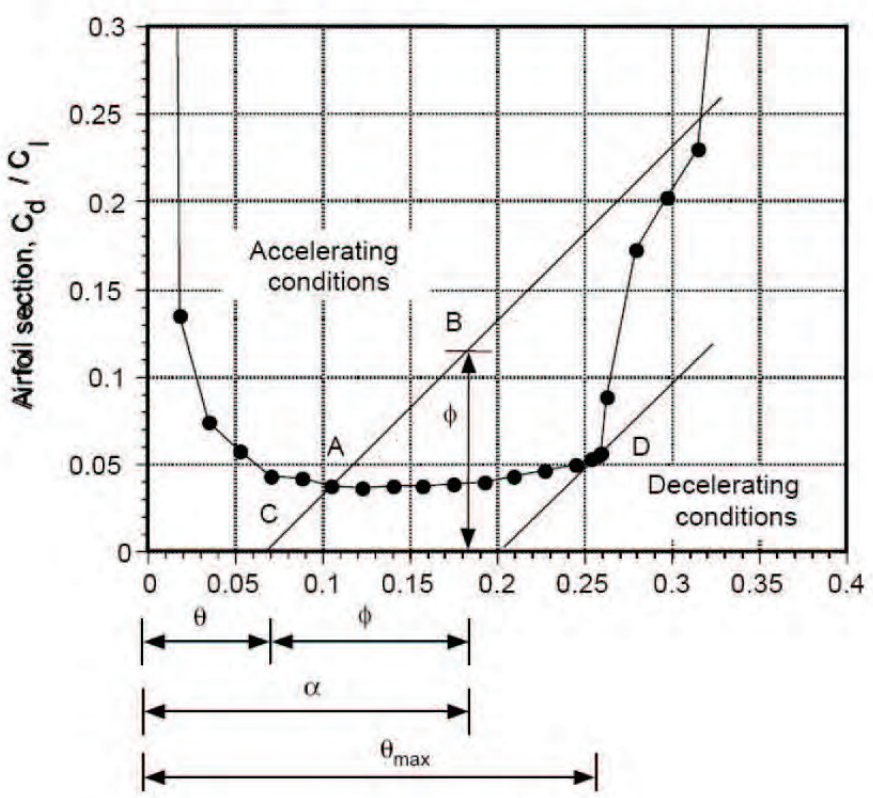

Figure 2.11: Blade Stall Wimperis Diagram. Reproduced from [4]

The resultant force coefficient defined as

$$C_r = \frac{\sqrt{L^2 + D^2}}{\frac{1}{2}\rho V_\infty^2 A} \tag{2.4}$$

is an important characteristic of the autogyro. Experimental data in Fig.2.12 shows that for angles-of-attack greater than 30 degrees the resultant force coefficient C_r is approximately 1.25. The drag coefficient, C_D, of a circular disk with a flow normal to its surface has a value of $C_D = 1.11$. Therefore, at high enough angles of attack, a disk in an autorotative state acts as a bluff body [4]. Using this phenomenon, it is possible to create a direct relationship to the descent velocity V_d of an autorotative craft.

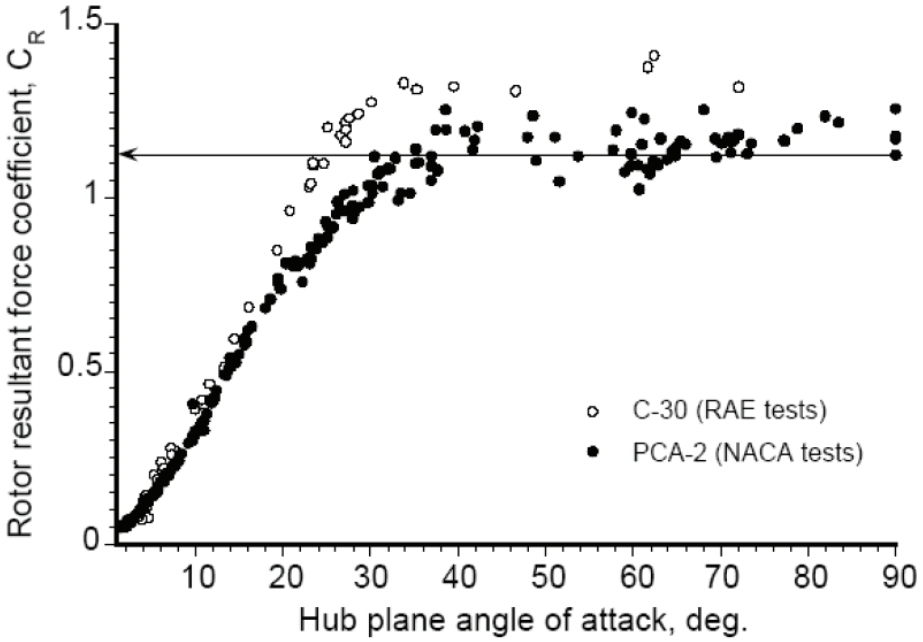

Figure 2.12: Coefficient of resultant force. Reproduced from [4]

The formulation for descent rate is derived in [48]. It is shown that the descent rate V_d of a vertically falling autogyro is

$$V_d = 25.94\frac{W}{A} \text{ (ft/s)} \tag{2.5}$$

where W is the weight of the craft and A the disk area. Tests done in [49, 50] were used to find the rate of descent with respect to forward speed during gliding flight and are shown in Fig.2.13. The rate of descent V_d reaches a minimum around $V_f/v_h = 2$ and increases thereafter due to increased drag.

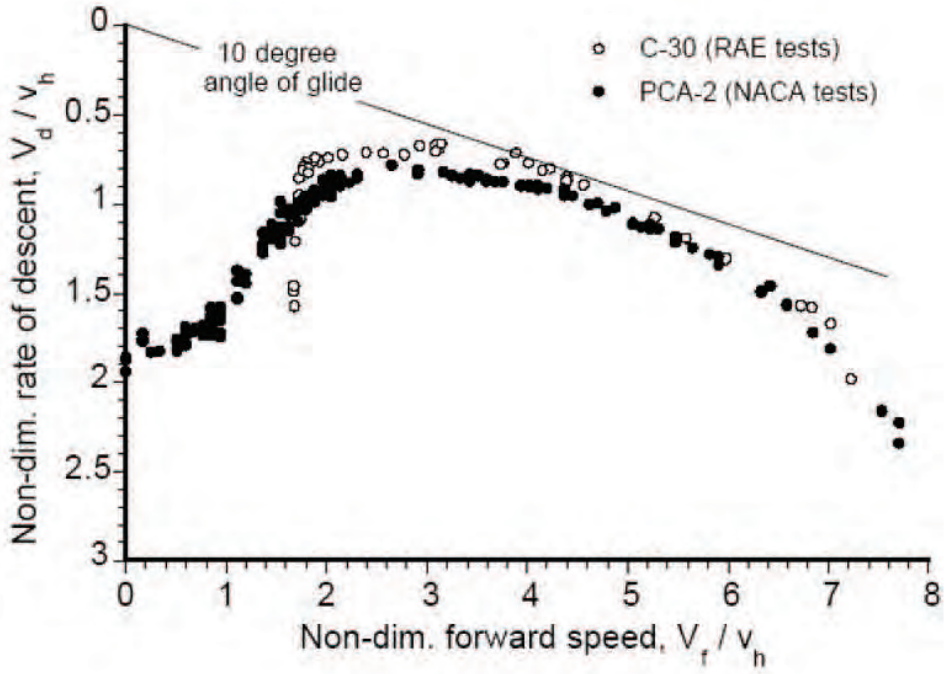

Figure 2.13: Nondimensional descent rate vs nondimensional forward speed in autorotational gliding flight. Reproduced from [4]

With the advent of the flapping hinge and lead-lag hinge, the gyroplane was finally able to sustain level flight. However, around the 1950's helicopters came into the forefront and gyroplanes were given less importance. Only recently have gyroplanes gained increased interest leading to advanced dynamic models of rotors and airflow [51, 52, 53, 54, 55].

2.3 Summary

Although there exists many designs for AWEs, autorotation based energy extraction remains relatively unexplored from a theory perspective. Autorotation has been shown to be a safe way to enable low-speed flight and allow for safe landings under engine failure because of its natural conversion of potential energy to lift [16, 56]. Even though lighter-than-air or

aerostat devices appear alluring at first glance, a review of the technology shows difficulty in not only maneuverability but having to rely on high tether tension to stay in place. By utilizing a more maneuverable system that can control the magnitude and direction of its lift the reliance on tether tension can be minimized.

Clearly the autogyro provides a unique way of achieving lift that can be implemented to harvest energy. Expanding on the literature, it is possible to develop a new autogyro model focused on energy extraction. This model predicts the behavior of an autogyro under regenerative torque and calculate the approximate energy that can be collected.

CHAPTER 3: MODEL OF STEADY AUTOROTATION

The first models of steady autorotation were developed by Glauert and Wheatley in the early 1930s, [17, 6]. These models provided a basis of autorotation theory and introduced the Blade Element Momentum method. The Blade Element Momentum (BEM) method is the foundation of autorotation theory. The theory discretizes a rotor blade to thin strips, the forces are analyzed at each strip and integrated through the blade-span. The forces are then averaged over one full rotation. The BEM approach in [6] derives the thrust T and rotor torque Q for a rotor at an angle of incidence α translating at a speed V. An inertially fixed rotor in a wind field with wind velocity V is assumed for which the same analysis is applicable - see Fig.1.4(a). The analysis assumes that the flapping angle of each blade, β, is a periodic function of the blade's angular position $\psi(\dot{\psi} = \Omega)$, which naturally leads to the use of a Fourier series [17, 6, 39, 40]. For multi-blade systems the flapping angle of each blade is assumed phase-shifted in ψ from the other blades, Fig.3.1. Sign convention and variables are defined in Fig.3.1.

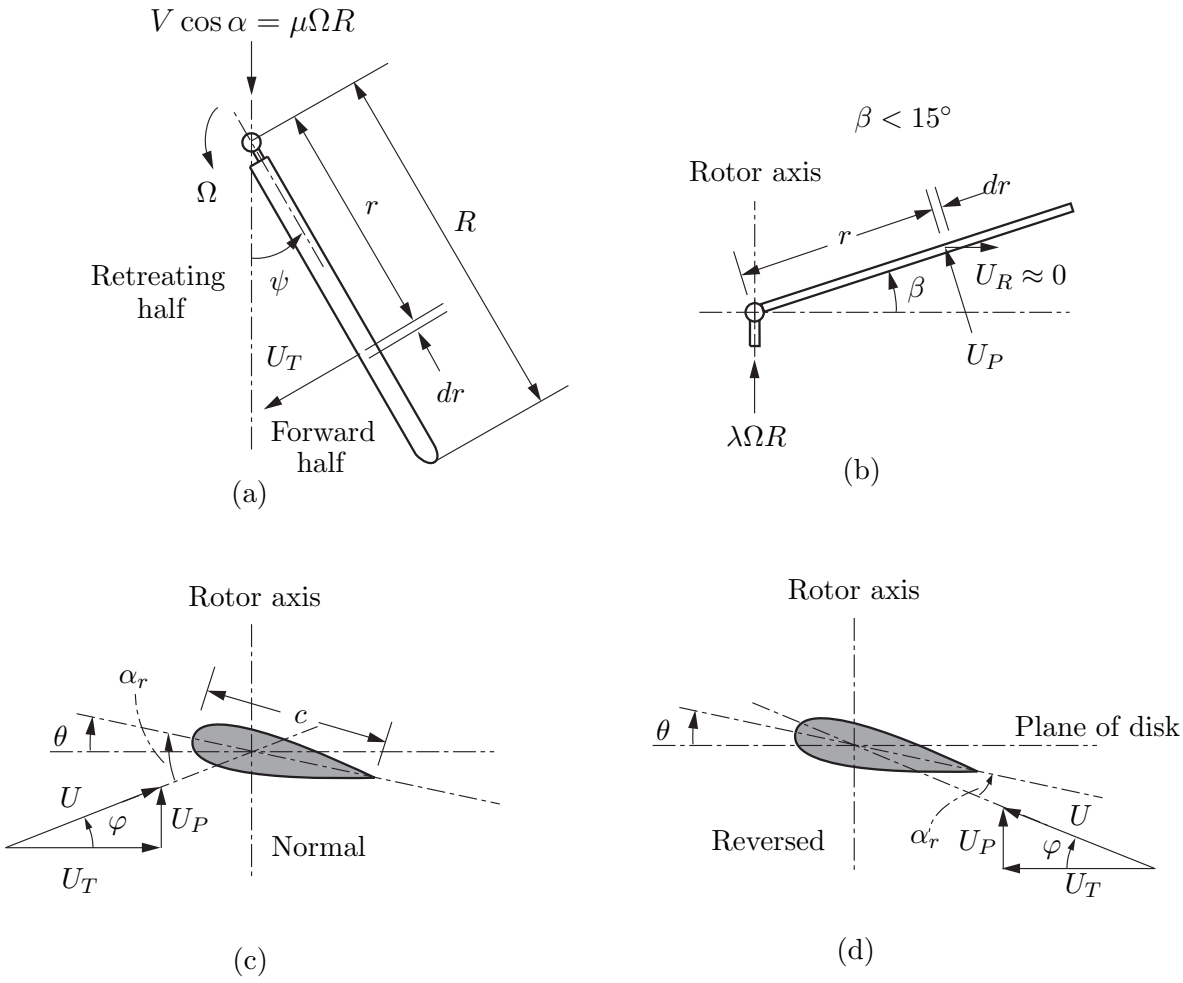

Figure 3.1: Blade element views: (a) Along spin axis, (b) Flapping motion, (c) Cross-sectional view, (d) Reversed Velocity Region

At steady autorotation, blade motion is taken to be identically cyclic at each rotation, therefore, the motion can be expressed as a Fourier series of the form

$$\beta = a_0 - a_1 \cos\psi - b_1 \sin\psi - a_2 \cos 2\psi - b_2 \sin 2\psi ... \tag{3.1}$$

where a_0, a_1, b_1, a_2, b_2 are Fourier coefficients to be determined. The coefficient expressions are listed in section B and detailed derivations are provided in [6]. To quantify the overall

rotor speed, the tip speed ratio and inflow ratio,

$$\mu = \frac{V\cos\alpha}{\Omega R}, \qquad \lambda = \frac{V\sin\alpha - \nu}{\Omega R} \tag{3.2}$$

are introduced where ν is the downward induced velocity from the rotor blades. Using the same analogy as airfoil theory, the induced velocity can be expressed as

$$\nu = \frac{T}{2\pi R^2 \rho V'}, \qquad V'^2 = (V\sin\alpha - \nu)^2 + V^2\cos^2\alpha \tag{3.3}$$

which can consolidate to

$$\tan\alpha = \frac{\lambda}{\mu} + \frac{\frac{1}{2}C_T}{\mu(\lambda^2+\mu^2)^{1/2}}, \qquad C_T = \frac{T}{\rho\Omega^2\pi R^4} \tag{3.4}$$

The wind velocity is broken down into three directions U_T, U_P, and U_R. Where U_T is parallel to the rotor disk and perpendicular to the center of rotation and blade span. U_P is defined as parallel to the center of rotation and perpendicular to U_T, and, finally, U_R is parallel to the blade and perpendicular to U_T. Referring to Fig.3.1(a,b) and to [6] the velocities can be expressed as

$$\begin{aligned} U_T &= \Omega r + \mu\Omega R\sin\psi, \qquad U_R = \mu\Omega R\cos\psi + \lambda\Omega R\sin\beta \\ U_P &= \lambda\Omega R\cos\beta - r\frac{dB}{dt} - \mu\Omega R\sin\beta\cos\psi \end{aligned} \tag{3.5}$$

Also note that for small angles of attack $U_T = U\cos\varphi = U$ and $U_P = U\sin\varphi = U\varphi$. For the reversed flow region shown in Fig.3.1(a) only a small portion of the blade creates lift and the remaining section is in stall. That region is from $B \cdot R$ to the point U_T is equal to 0 or approximately $-\mu R\sin\psi$. Variable B represents a fractional term to account for blade-tip losses. Finally, the lift-coefficient is taken to be the same as an airfoil, $C_L = a\alpha_r$ where a is

the lift-curve slope and α_r is the angle of attack of the wing at distance r from the flapping hinge. In [6] the blade pitch, θ, is taken to be linearly varying, therefore $\alpha_r = \theta_0 + \frac{r}{R}\theta_1 + \varphi$ where θ_0 is the initial pitch and θ_1 is the slope of the varying pitch.

Now that the fundamental characteristic equations have been laid down the thrust (T) can be analyzed. The thrust is broken down into the reverse (blade-retreating) and forward (blade-advancing) flow regions and is computed as follows

$$
\begin{aligned}
T &= \frac{b}{2\pi}\int_0^{2\pi} d\psi \int_0^{BR} \frac{1}{2}\rho c U^2 C_L dr = \frac{b}{2\pi}\int_0^{2\pi} d\psi \int_0^{RB} \frac{1}{2}\rho c a U^2 \left(\theta_0 + \frac{r}{R}\theta_1 + \varphi\right) dr \\
&+ \frac{b}{2\pi}\int_\pi^{2\pi} \left[\int_{-\mu R\sin\psi}^{BR} \frac{1}{2}\rho c a U^2 \left(\theta_0 + \frac{r}{R}\theta_1 + \varphi\right) dr + \int_0^{-\mu R\sin\psi} \frac{1}{2}\rho c a U^2 \left(-\theta_0 - \frac{r}{R}\theta_1 - \varphi\right) dr\right] d\psi \\
&= \frac{1}{2} bc\rho a \Omega^2 R^3 \left\{\frac{1}{2}\lambda\left(B^2 + \frac{1}{2}\mu^2\right) + \theta_0\left(\frac{1}{3}B^3 + \frac{1}{2}\mu^2 B - \frac{4}{9\pi}\mu^3\right)\right. \\
&\left. + \theta_1\left(\frac{1}{4}B^4 + \frac{1}{4}\mu^2 B^2 - \frac{1}{32}\mu^4\right) + \frac{1}{4}\mu^2 b_2 B + \frac{1}{8}\mu^3 a_1\right\}
\end{aligned}
\tag{3.6}
$$

where c is the blade chord length, θ is the blade pitch, and λ is the axial speed ratio. A further look at thrust is done in section 3.2. Using Eqs.3.4 and 3.6 it is possible to obtain a non-dimensionalized thrust equation. Utilizing C_T, the author in [6] shows that the lift coefficient C_{L_r} can be defined as

$$
C_{L_r} = \frac{2C_T \cos\alpha^3}{\mu^2} \tag{3.7}
$$

The author also derives the lift-drag ratio by analyzing the energy loss from dissipation and thrust generation. The energy loss integral in [6] is then used to derive

$$
\frac{D_r}{L_r} = \frac{\sigma\delta\left(1 + 3\mu^2 + \frac{3}{8}\mu^4\right)}{8\mu C_T} + \frac{1/2C_T}{\mu\left(\mu^2 + \lambda^2\right)^{1/2}} \tag{3.8}
$$

The aerodynamic forces on a blade creates a moment that is given by

$$M_T = \int_0^{BR} \frac{1}{2}\rho c U^2 C_L r dr = \int_0^{BR} \frac{1}{2}\rho c a \left\{ \left(\theta_0 + \frac{r}{R}\theta_1\right) U_T^2 + U_T U_P \right\} r dr$$
$$- 2\int_0^{-\mu R \sin\psi} \frac{1}{2}\rho c a \left\{ \left(\theta_0 + \frac{r}{R}\theta_1\right) U_T^2 + U_T U_P \right\} r d_P \tag{3.9}$$

where the second half of the equation only comes into consideration from $[\pi, 2\pi]$. As the wind flows through the rotor disk it experiences a torque. For b blades, the average aerodynamic torque is

$$\begin{aligned} Q_e &= \frac{b}{2\pi}\int_0^{2\pi} d\psi \int_0^{BR} \frac{1}{2}\rho c U^2 \phi C_L r dr - \frac{b}{2\pi}\int_0^{2\pi} d\psi \int_0^{R} \frac{1}{2}\rho c U^2 \delta r dr \\ &= \frac{b\rho c\Omega^2 R^4 a}{2}\lambda^2\left(\frac{1}{2}B^2 - \frac{1}{4}\mu^2\right) + \lambda\left(\frac{1}{3}\theta_0 B^3 + \frac{2}{9\pi}\mu^3\theta_0 + \frac{1}{4}\theta_1 B^4 + \frac{1}{32}\mu^4\theta_1\right) \\ &\quad + \mu\lambda a_1\left(\frac{1}{2}B^2 - \frac{3}{8}\mu^2\right) + a_0^2\left(\frac{1}{4}\mu^2 B^2 - \frac{1}{16}\mu^4\right) - \frac{1}{3}\mu a_0 b_1 B^3 + a_1^2\left(\frac{1}{8}B^4 + \frac{3}{16}\mu^2 B^2\right) \\ &\quad + b_1^2\left(\frac{1}{8}B^4 + \frac{1}{16}\mu^2 B^2\right) - a_2\left(\frac{1}{4}\mu^2 a_0 B^2 + \frac{1}{6}\mu b_1 B^3\right) + \frac{1}{2}a_2^2 B^4 \\ &\quad + b_2\left(\frac{1}{8}\mu^2\theta_0 B^2 + \frac{1}{12}\mu^2\theta_1 B^3 + \frac{1}{6}\mu a_1 B^3\right) + \frac{1}{2}b_2^2 B^4 - \frac{\delta}{4a}\left(1 + \mu^2 - \frac{1}{8}\mu^4\right) \end{aligned} \tag{3.10}$$

where for steady autorotation $Q_e = 0$.

The tip-speed ratio, an equilibrium point of the system, μ, Eq.3.2, must be known beforehand, making this model inherently difficult to use. In this application, only the wind velocity V and generator torque Q_e are known. The proposed dynamic model removes this constraint and allows the system equations to reach its own equilibrium, at which point the steady-state tip-speed μ can be extracted. The model developed by [6] is used to create a basis for comparison to test the dynamic model of autorotation presented in chapter 4. To establish the validity of the code, a simulation was run to compare the results of the theoretical and experimental data presented in [6].

3.1 Initial Validation Results

Three main performance variables: rotor lift coefficient (C_{L_r}), thrust coefficient (C_T), and the flapping and coning coefficients (a_0, a_1, a_2, b_1, b_2) are used to validate this model. To create a basis for comparison, the constants defined in [6] are listed in table 3.1 and appendix C.1 are utilized. An important assumption was made in [6] that effectively neglected the blade weight, specifically the term $\frac{M_w}{I\Omega^2}$ greatly effecting the equation a_0 found in appendix B. The blade weight is neglected because the rotational speed is sufficiently high such that the moment due to the blade weight is effectively negligible. This oversight was found through thorough inspection of the equations and simulations. Another caveat is from how the procedure was set to calculate the Fourier coefficients. The non-dimensional values of μ & λ (Eq.3.2) are lumped parameters that are inputs to all the functions. Due to this lumped parameter, the value of Ω is unknown and thus must be calculated along the way. Variables Ω and a_0 must be solved simultaneously, which was originally avoided in [6] through approximation. An iterative method is proposed to show that with sufficiently high wind speeds V, where V and Ω are proportional, the results from [6] can be reproduced but with the constraint of high rotational speed removed; as that is something this application of autorotation cannot assume.

Table 3.1: Simulation parameters from [6]

Parameter	Value	Description
θ_0	0.0384	Blade pitch at root (rad)
θ_1	1.256×10^{-4}	Slope of blade pitch (rad/in)
ρ	0.00210	Air density (slugs/ft^3)

In this validation, the assumption of high rotational speed is retained, therefore the blade moment M_w is neglected by and the simulation results are compared with those presented in [6]. The results in Fig.3.2 show that the simulation was correctly developed to the standards

presented in [6]. Moving forward, the assumption of high rotational speed Ω is removed and M_w is reincorporated. This requires a change in the solving procedure since the approximation no longer holds and all the values must now be solved simultaneously. The new approach uses a numerical iteration technique as follows:

(a) Provide a tip-speed ratio μ and Generator Torque Q_e

(b) Guess initial values for α, Ω, and λ

(c) While $\Delta\alpha$ and $\Delta\Omega$ are greater than ϵ loop through steps d-k.

(d) Substitute in the physical constants and μ into the flapping coefficients and obtain a_0, a_1, a_2, b_1, b_2

(e) Set Q_e on Eq.3.10 to retrieve λ

(f) Utilize λ and μ to calculate C_T with Eq.3.12

(g) Using Eq.3.4 calculate α

(h) Next calculate the lift-drag ratio $\frac{D_r}{L_r}$ using Eq.3.8

(i) Calculate lift-coefficient C_{L_r} using Eq.3.7

(j) Using the lift-drag ratio Eq.3.8 and lift-coefficient Eq.3.7 calculate C_{D_r}

(k) To find the required wind velocity for steady autorotation, set the lift-force to the weight W and use the following equation

$$V_\eta = \sqrt{\frac{W}{\frac{1}{2}\rho\pi R^2 C_{L_T}}} \tag{3.11}$$

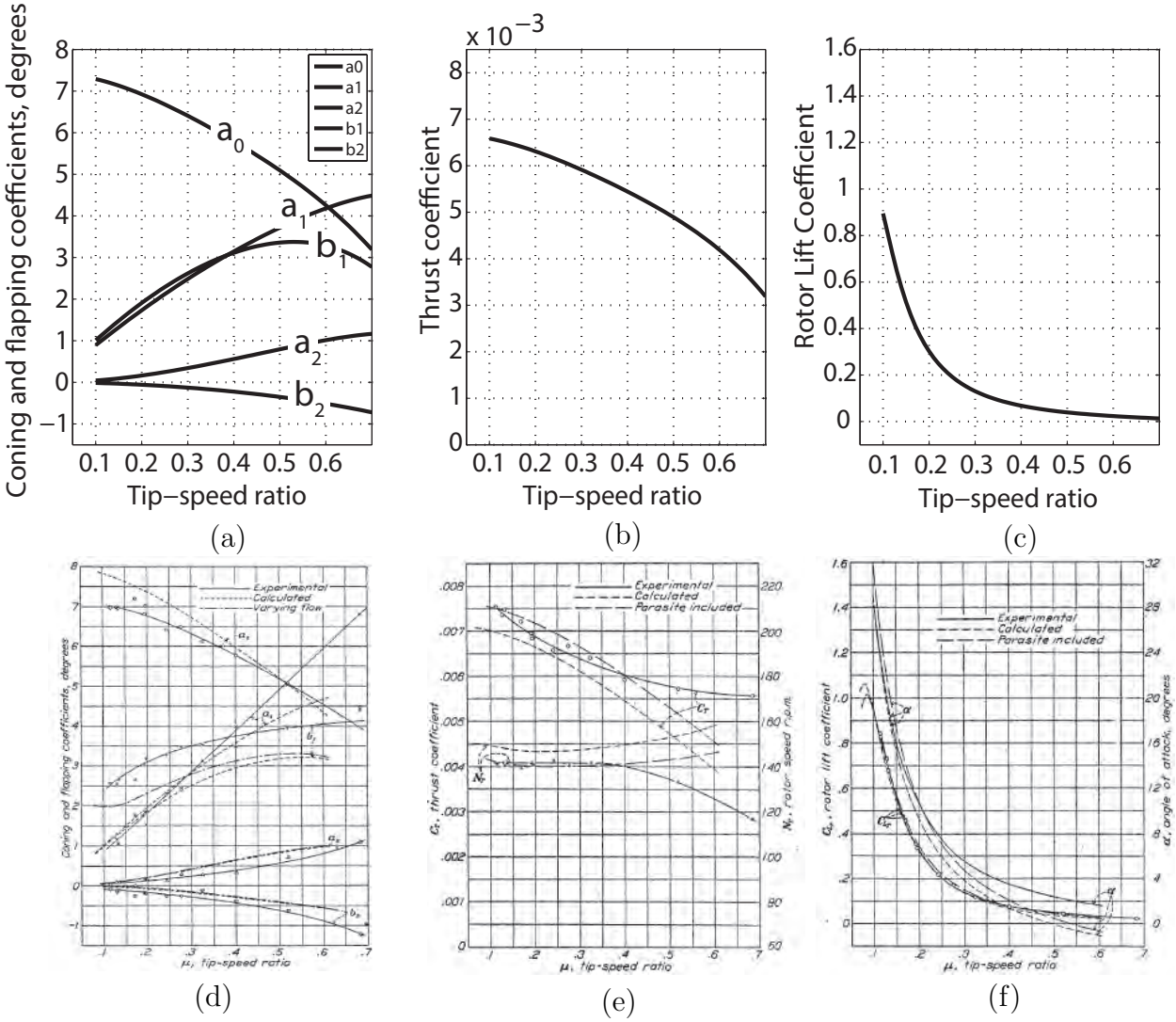

Figure 3.2: (a) Flapping and Coning Coefficients (b) Thrust Coefficient (c) Lift Coefficient (d) Flapping and Coning Coefficients from [6] (e) Thrust Coefficient from [6] (f) Lift Coefficient from [6]

As a note the BEM method is not valid for climb velocity ratios of $-2 \leq \frac{V_c}{V_h} \leq 0$ [16]. Simulations past ≥ 0.5 do not provide meaningful results as momentum theory is no longer valid in this region because of turbulent airflow depicted in Fig.3.5. The initial simulation uses extremely high wind speeds of (~ 500 ft/s) to show that the iterative model converges to the model presented in [6]. Proceeding forward, a simulation with wind speeds of (~ 70

ft/s) is completed, which is more realistic to what an autogyro will experience in an energy harvesting application.

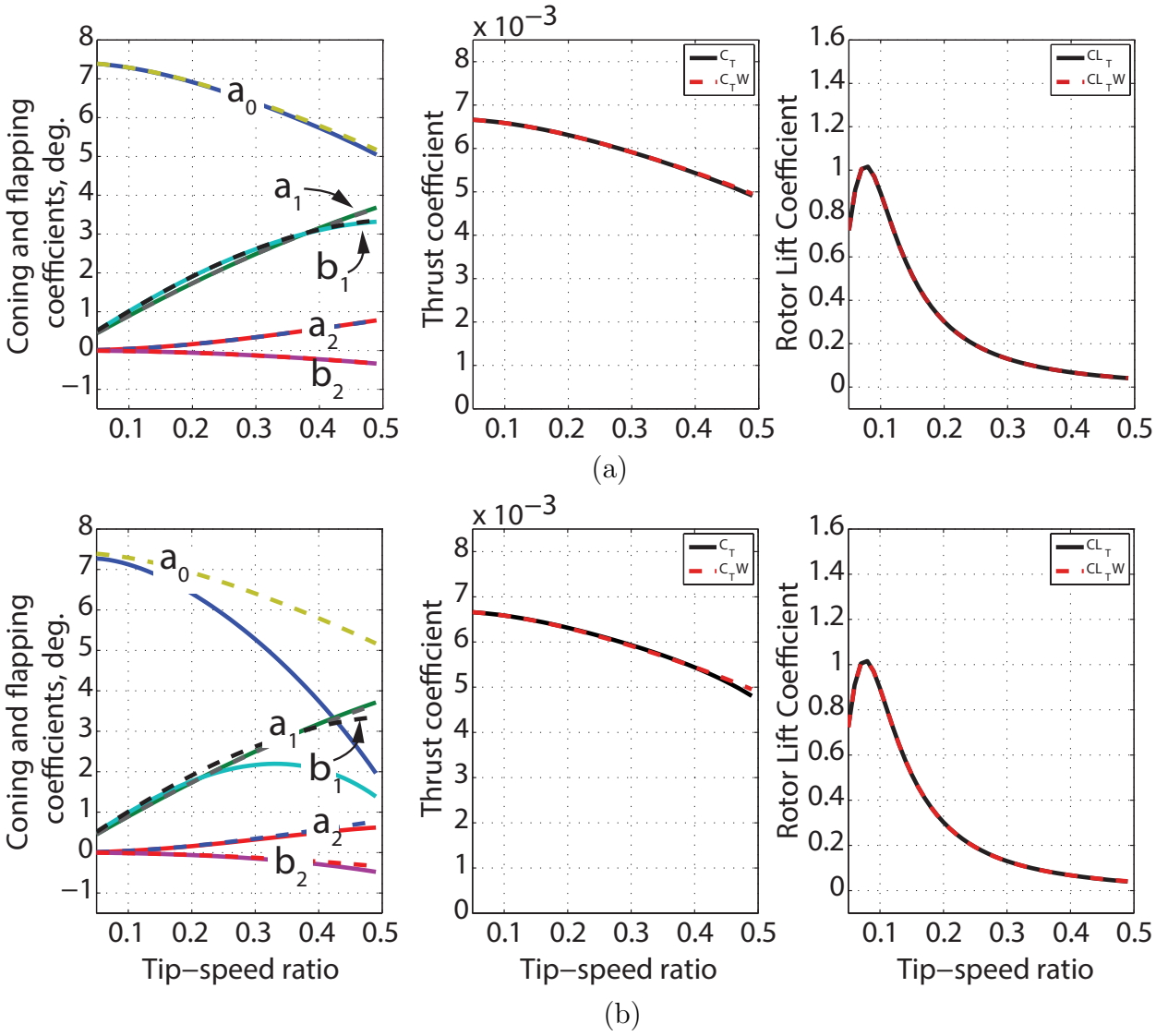

Figure 3.3: (a) Iterative method with V=500 ft/s (b) Iterative method with V=70 ft/s

The results show that at lower wind speeds of around ($\sim 70ft/s$) the Fourier coefficients diverge from the standard model developed in [6]. However, the thrust and lift coefficients C_T and C_{L_r}, respectively, are not greatly affected. With the verification of the model characteristics of an autogyro at different equilibria μ are analyzed.

In Fig.3.4 the lift coefficient, drag coefficient and required wind speed to maintain lift are shown for different tip-speeds. The required wind speed is shown for zero regenerative torque or generator load. The minimal wind speed required to maintain flight is around $13m/s$ or $\sim 42ft/s$ at a tip-speed of 0.08. At this region drag is also at its maximum. Closer to a tip-speed of 0.09 the lift coefficient is at its maximum, which is a region that requires more energy to sustain. Shown in chapter 4 these tip-speeds are unlikely to be reached as most simulation results lie around $\mu \approx .11$.

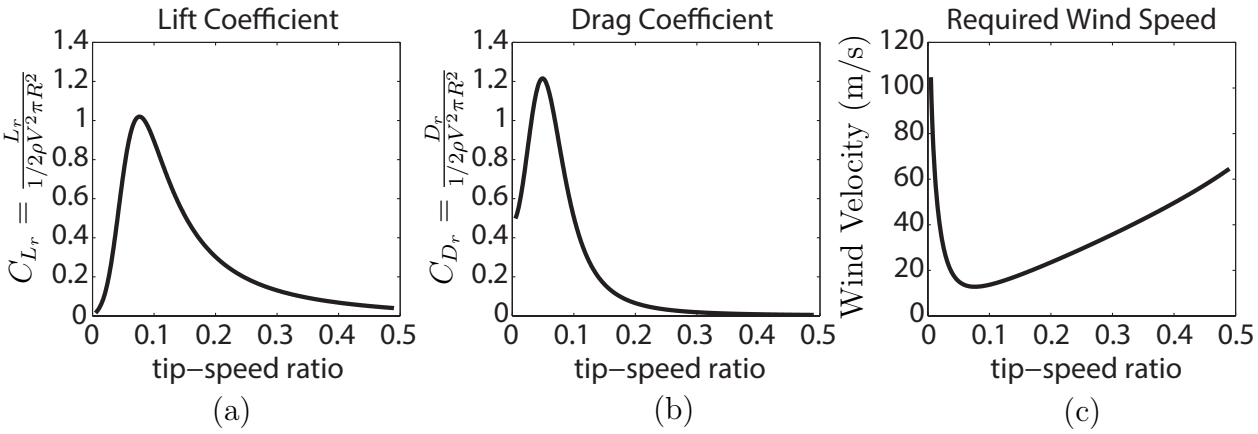

Figure 3.4: (a) Lift Coefficient (b) Drag Coefficient (c) Wind velocity required to maintain level flight

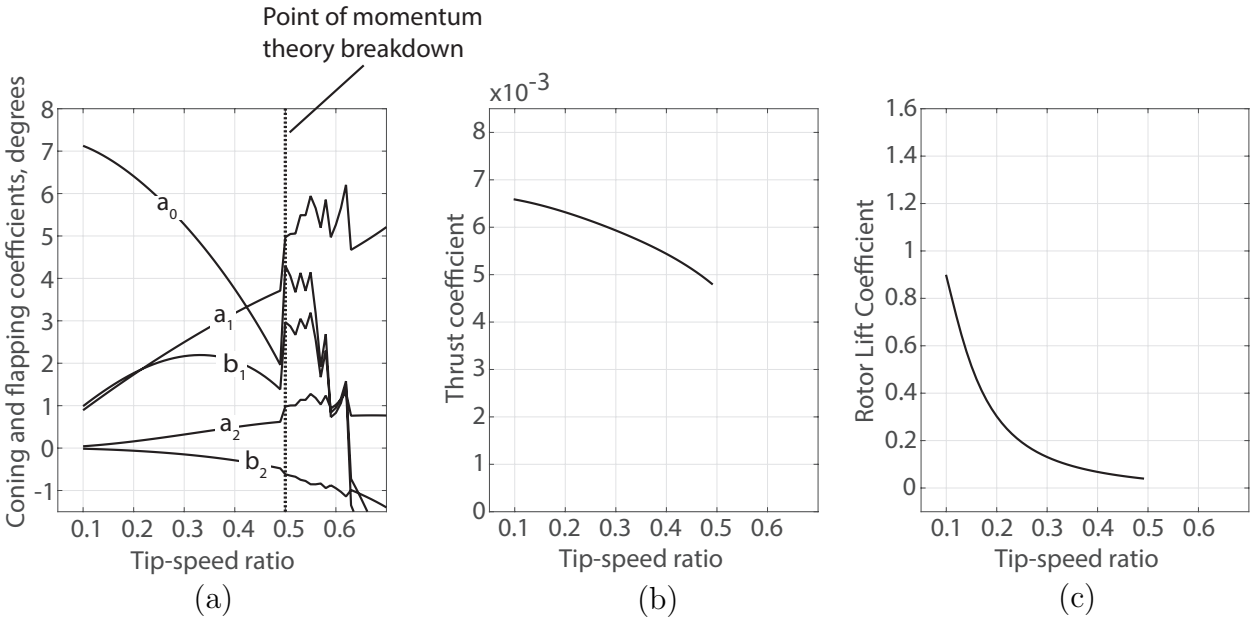

Figure 3.5: (a) Lift Coefficient (b) Drag Coefficient (c) Wind velocity required to maintain level flight

3.2 Thrust Coefficient

With the verification of the simulation model, a visual look into how flapping blades affect autorotation is studied. This is accomplished by analyzing the thrust coefficient of a single blade at every point as it rotates from $0 - 2\pi$ and compare it to autorotation that occurs without flapping. The thrust coefficient is defined as $C_T \triangleq \frac{T}{\rho\Omega^2\pi R^4}$, therefore the thrust T becomes

$$C_T = \frac{1}{2}\sigma a \left\{ \frac{1}{2}\lambda\left(B^2 + \frac{1}{2}\mu^2\right) + \theta_0\left(\frac{1}{3}B^3 + \frac{1}{2}\mu^2 B - \frac{4}{9\pi}\mu^3\right) + \theta_1\left(\frac{1}{4}B^4 + \frac{1}{4}\mu^2 B^2 - \frac{1}{32}\mu^4\right) + \frac{1}{4}\mu^2 b_2 B + \frac{1}{8}\mu^3 a_1 \right\} \tag{3.12}$$

where $\sigma = \frac{bc}{\pi R}$.

By setting the Fourier coefficients $(a_0, a_1, a_2, b_1, b_2)$ to zero, the flapping component of Eq.3.12 is effectively removed. Fig.3.6 shows a comparison of flapping versus no flapping at different equilibria or tip-speed ratios. With no flapping in Figs.3.6d,e,f, the forward thrust region shows higher thrust coefficients. This thrust imbalance is important to combat in order to achieve level flight and flapping is a simple and effective way of achieving that. With flapping, Figs.3.6a,b,c, the thrust coefficients even out as regions of the forward half show decreased life and regions of the reverse half show increased lift. Note that as tip-speed decreases the two regions balance out because the rotational speed is much higher than the forward wind velocity. This occurs because the local wind velocities experienced by the blades become virtually the same. Juan de la Cierva used a hinge to achieve flapping but todays gyroplanes use a teeter-toter system with composite material blades. This achieves the same result with simpler,lighter mechanics. The aeroelastic behavior of these blades are modeled in [51]. Now with a thorough understanding of the steady-state characteristics of autorotation, an analysis of dynamic autorotation can be developed.

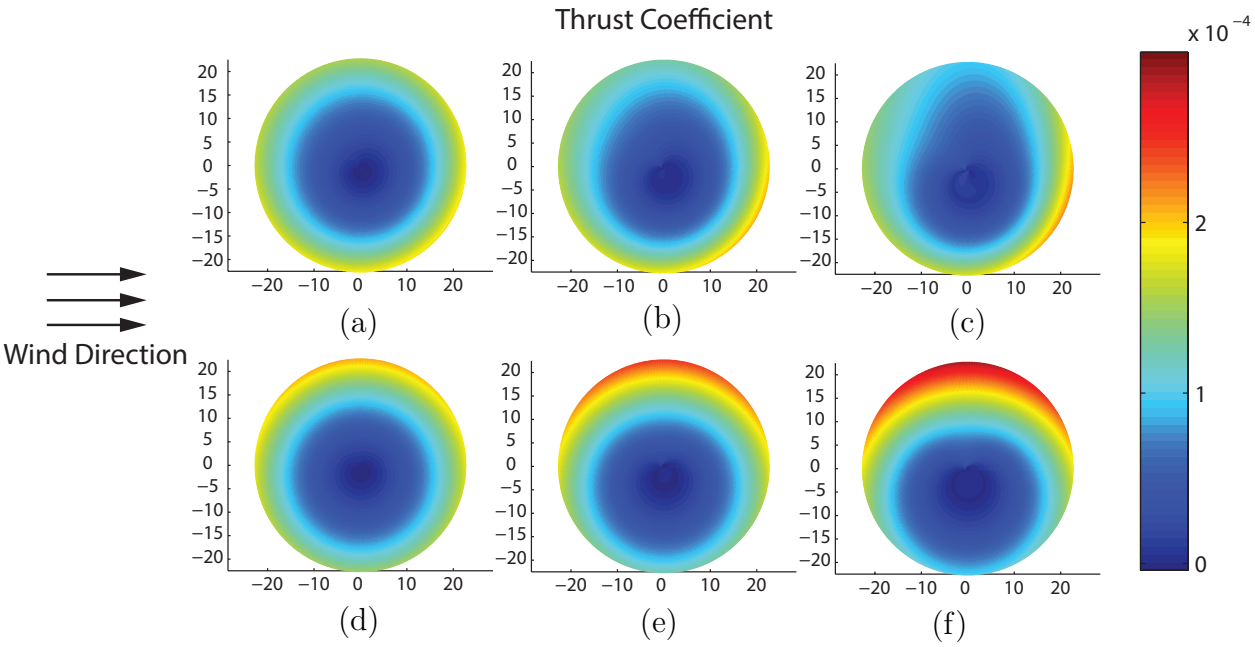

Figure 3.6: Wind coming in from left of page (a) $\mu = 0.2$ (b) $\mu = 0.4$ (c) $\mu = 0.6$ (d) $\mu = 0.2$ with no flapping (e) $\mu = 0.4$ with no flapping (f) $\mu = 0.6$ with no flapping

CHAPTER 4: AUTOROTATION DYNAMIC MODEL

The phenomenon of autorotation is inherently dynamic because of it's complex interaction between the air and the falling rotor. Allowing the rotor blades to flap adds additional degrees of freedom, complicating the dynamics further. Although [6] analyzes the flapping at steady state, everything leading up to steady state is unknown. Even at steady-state the torque and thrust fluctuations are not modeled. By studying the interaction of a four-bladed autogyro in a static wind field, Fig.4.1, insights can be made with respect to the transient behavior. For simplicity and to compare the final steady-state solutions with [6] the radius of the hub ($r_h = 0$) is neglected. Also the twisted blade design used in [6] is removed and instead a uniform blade is used to simplify several equations.

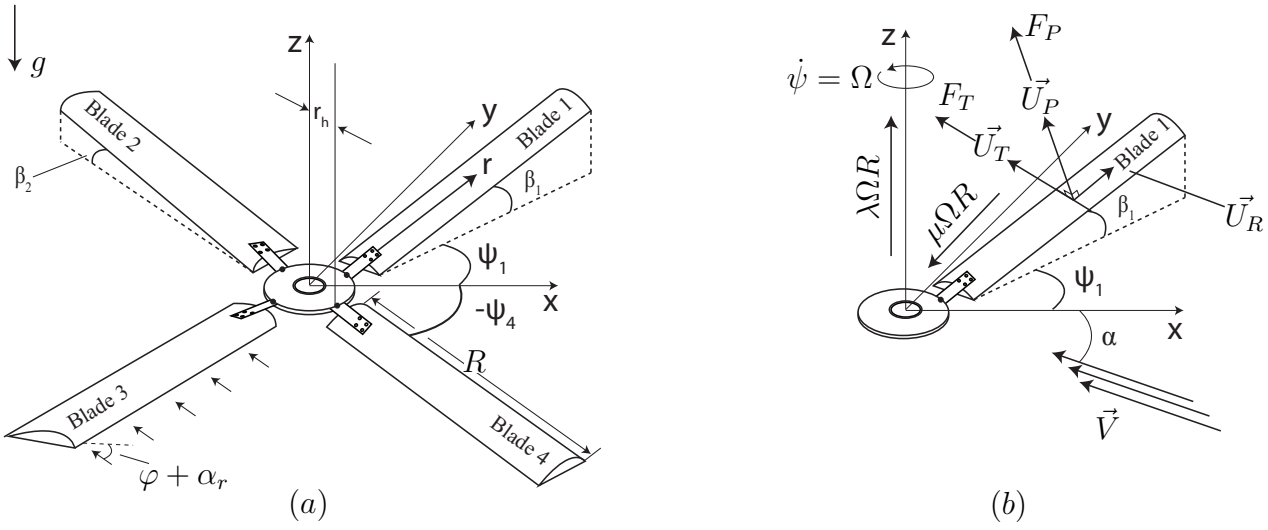

Figure 4.1: Dynamic Model: (a) Complete Autogyro System (b) Effect of Rotation on Blade 1

Lagrangian dynamics are used to model the autogyro shown in Fig.4.1. The kinetic energy (T) and the potential energy (V) terms are first derived to yield the Lagrangian $L = T - V$. The angles ψ_i and β_i, where $i = 1, 2, 3, 4$, represent the generalized coordinates of rotation

and flapping, respectively, of each blade as shown in Fig.4.1. The angle ψ_i represents the rotation of the blade along the plane $x-y$ parallel to the hub. The angle of inclination, β_i, of a blade is measured from the $x-y$ plane of the body fixed axis. The total kinetic energy of the system can be described as the sum of the rotational and translation energy terms of the four blades. For one blade the kinetic energy is

$$T_i = \frac{1}{2} m_b \dot{\vec{r}}_{a_i} \cdot \dot{\vec{r}}_{a_i} + \frac{1}{2} \vec{\omega}_{r_i} \cdot \vec{H}_{G_i}, \quad \dot{\vec{r}}_{a_i} = \dot{\vec{r}}_i + \vec{\omega}_{r_i} \times \vec{r}_i \tag{4.1}$$

where $\dot{\vec{r}}_{a_i}$ represents the velocity vector relative to the body fixed axis from the center of rotation to the center of the blade. The hub radius is ignored, therefore, the velocity vector equates to the time rate of change of the position vector from the center of rotation to the center of the blade.

The absolute position vector $\vec{r}_{a_i}$, angular speed $\vec{\omega}_{r_i}$, and momentum $\vec{H}_{G_i}$ are

$$\vec{r}_{a_i} = \frac{R}{2} \cos\beta_i \cos\psi_i \hat{\mathbf{i}} + \frac{R}{2} \cos\beta_i \sin\psi_i \hat{\mathbf{j}} + \frac{R}{2} \sin\beta_i \hat{\mathbf{k}} \tag{4.2}$$

$$\vec{\omega}_{r_i} = \dot{\psi}_i \sin\beta_i \hat{\mathbf{i}} + \dot{\beta}_i \hat{\mathbf{j}} + \dot{\psi}_i \cos\beta_i \hat{\mathbf{k}} \tag{4.3}$$

$$\vec{H}_{G_i} = I_{xx} \dot{\psi}_i \sin\beta_i \hat{\mathbf{i}} + I_{yy} \dot{\beta}_i \hat{\mathbf{j}} + I_{zz} \dot{\psi}_i \cos\beta_i \hat{\mathbf{k}} \tag{4.4}$$

where the inertias I_{xx}, I_{yy}, and I_{zz} of the blade are approximated as a cuboid, Appendix A.

Therefore taking the derivative of Eq.4.2 and substituting Eqs.4.2,4.3, and 4.4 into Eq.4.1,

the kinetic energy of a single blade is

$$T_i = \frac{R^2}{8} m_b \dot{\beta_i}^2 + \frac{R^2}{2} m_b \dot{\psi_i}^2 \cos^2 \beta_i + \frac{I_{xx}}{2} \dot{\psi_i}^2 \sin^2 \beta_i + \frac{I_{yy}}{2} \dot{\beta_i}^2 + \frac{I_{zz}}{2} \dot{\psi_i}^2 \cos^2 \beta_i \tag{4.5}$$

and the potential energy is

$$V_i = \frac{R}{2} m_b g \cos \beta_i \tag{4.6}$$

Considering only blade 1, the Lagrangian formulation becomes

$$\frac{d}{dt}\left(\frac{\partial L}{\partial \dot{\psi_1}}\right) - \frac{\partial L}{\partial \psi_1} = Q_{\psi_1} \tag{4.7}$$

$$\frac{d}{dt}\left(\frac{\partial L}{\partial \dot{\beta_1}}\right) - \frac{\partial L}{\partial \beta_1} = Q_{\beta_1} \tag{4.8}$$

After differentiating and simplifying the equation of motion of blade 1 for rotation is

$$\left[(R^2 m_b + I_{zz}) \cos^2 \beta_1 + I_{xx} \sin^2 \beta_1\right] \ddot{\psi} + \left[I_{xx} - I_{zz} - R^2 m_b\right] \dot{\psi} \dot{\beta_1} \sin 2\beta_1 = Q_{\psi_1} \tag{4.9}$$

and the equation of motion for flapping is

$$\left[\frac{R^2}{4} m_b + I_{yy}\right] \ddot{\beta_1} - \frac{1}{2}\left[I_{xx} - I_{zz} - R^2 m_b\right] \dot{\psi}^2 \sin 2\beta_1 + \frac{R}{2} m_b g \cos \beta_1 = Q_{\beta_1} \tag{4.10}$$

where Q_{ψ_1} and Q_{β_1} are non-conservative aerodynamic forces causing blade rotation and flapping, respectively. Note that all blades have the same angular rotation velocity and acceleration along the $x - y$ plane, therefore, $\dot{\psi_1} = \dot{\psi_2} = \dot{\psi_3} = \dot{\psi_4}$ and $\ddot{\psi_1} = \ddot{\psi_2} = \ddot{\psi_3} = \ddot{\psi_4}$ therefore the index i is removed for these variables.

In the steady state model the flapping angle, β_i, is assumed to be small because the cen-

tripetal accelerations are much higher than the blade weight. The motion of the blades is unknown under unsteady dynamics, therefore the approximations originally made in [6] must be removed in the tangential wind speed U_T and perpendicular wind speed U_P. This leads to the expressions

$$U_T = \Omega r + \mu\Omega R \sin\psi_i, \qquad U_P = \lambda\Omega R\cos\beta_i - r\dot{\beta}_i - \mu\Omega R\beta_i \cos\psi_i \sin\beta_i \tag{4.11}$$

To determine Q_{ψ_1} and Q_{β_1} on blade 1 the forces are broken down with respect to the blade fixed axis. Two main forces are generated from the incoming wind. The first, F_T, is perpendicular to the blade span and parallel to the rotor disk. The second, F_P, is perpendicular to the blade span and to F_T shown in Fig.4.1b.

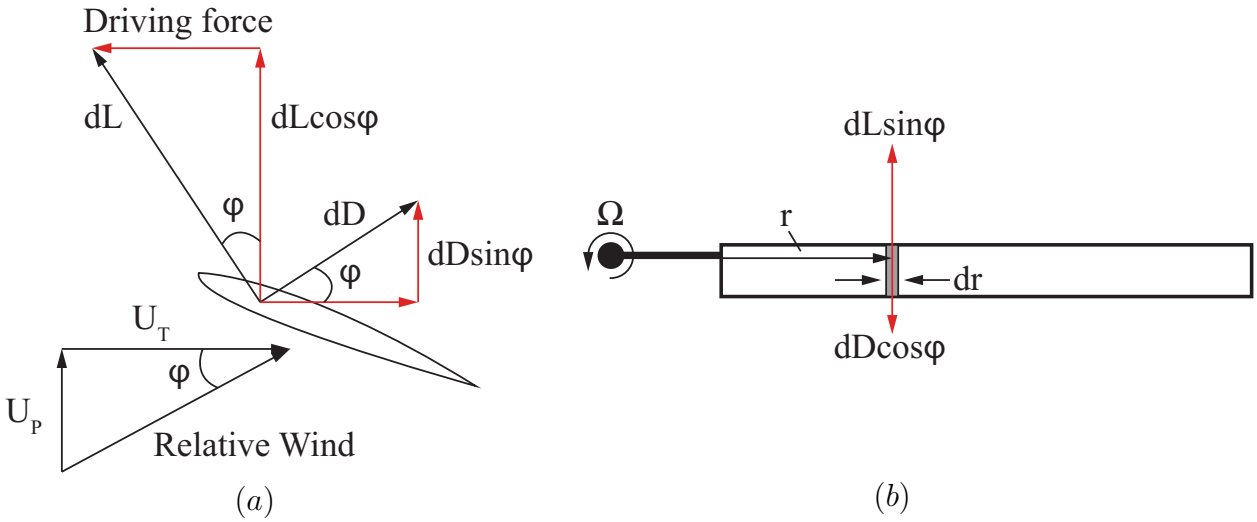

Figure 4.2: (a) Blade section forces (b) In-plane forces

The forces are derived from the components of lift L and drag D, Fig.4.2. The aerodynamic

forces a distance r from the blade root along the blade are

$$dF_T = dL\sin\varphi - dD\cos\varphi, \qquad dF_P = dL\cos\varphi + dD\sin\varphi \tag{4.12}$$

where φ is the angle of attack of the resultant velocity at a blade element with respect to the body fixed axis. Since U_T is much larger than U_P, Fig.4.1b, φ is assumed to be small. Therefore, the work done by the forces over a small displacement is $dW_T = (L\varphi r - dDr)d\psi$ and $dW_P = dLrd\beta$, where $dL = \frac{1}{2}\rho cU^2 C_L dr$ and $dD = \frac{1}{2}\rho cU^2\delta dr$. Accounting for the reverse velocity region and the methods in [6] the generalized forces can then be expressed as

$$Q_{\psi_1} = \begin{cases} \int_0^{BR} a\left[U_T U_P\theta_0 + U_p^2\right] r dr - \int_0^{R} \delta U_T^2 r dr & 0 \le \psi \le 2\pi \\ -2\int_0^{-\mu R\sin\psi} a\left[U_T U_P\theta_0 + U_p^2\right] r dr + 2\int_0^{-\mu R\sin\psi} \delta U_T^2 r dr & \pi \le \psi \le 2\pi \end{cases} \tag{4.13}$$

$$Q_{\beta_1} = \begin{cases} \int_0^{BR} a\left[U_T^2\theta_0 + U_p U_T\right] r dr & 0 \le \psi \le 2\pi \\ -2\int_0^{-\mu R\sin\psi} a\left[U_T^2\theta_0 + U_p U_T\right] r dr & \pi \le \psi \le 2\pi \end{cases} \tag{4.14}$$

The blades are assumed rigid and integrated along the blade length. This yields the equations of Q_ψ and Q_β found in appendix D. Q_ψ and Q_β are dependent on the inflow ratio λ. The value of λ is determined by combining Eqs.3.2,3.3 and solving for lambda. This results in the polynomial

$$\lambda^4 + \left(\mu^2 - \lambda_c^2\right)\lambda^2 + \lambda_c C_T\left(\mu^2 + \lambda^2\right)^{1/2} - \lambda_c^2\mu^2 - \frac{1}{4}C_T^2 \tag{4.15}$$

where $\lambda_c = \frac{V\sin\alpha}{\Omega R}$. Eq.4.15 is solved numerically.

The complete system equations are

$$\begin{aligned}&\left[(R^2 m_b + I_{zz})(\cos^2\beta_1 + I_{xx}\sin^2\beta_1 + \cos^2\beta_2 + I_{xx}\sin^2\beta_2 + \cos^2\beta_3 + I_{xx}\sin^2\beta_3\right.\\&\left.+\cos^2\beta_4 + I_{xx}\sin^2\beta_4)\right]\ddot{\psi} + \left[I_{xx} - I_{zz} - R^2 m_b\right]\Big[\dot{\psi}\dot{\beta}_1\sin 2\beta_1 + \dot{\psi}\dot{\beta}_2\sin 2\beta_2\\&+\dot{\psi}\dot{\beta}_3\sin 2\beta_3 + \dot{\psi}\dot{\beta}_4\sin 2\beta_4\Big] = Q_{\psi_1} + Q_{\psi_2} + Q_{\psi_3} + Q_{\psi_4}\end{aligned} \tag{4.16}$$

$$\left[\frac{R^2}{4}m_b + I_{yy}\right]\ddot{\beta}_1 - \frac{1}{2}\left[I_{xx} - I_{zz} - R^2 m_b\right]\dot{\psi}^2\sin 2\beta_1 + \frac{R}{2}m_b g\cos\beta_1 = Q_{\beta_1} \tag{4.17}$$

$$\left[\frac{R^2}{4}m_b + I_{yy}\right]\ddot{\beta}_2 - \frac{1}{2}\left[I_{xx} - I_{zz} - R^2 m_b\right]\dot{\psi}^2\sin 2\beta_2 + \frac{R}{2}m_b g\cos\beta_2 = Q_{\beta_2} \tag{4.18}$$

$$\left[\frac{R^2}{4}m_b + I_{yy}\right]\ddot{\beta}_3 - \frac{1}{2}\left[I_{xx} - I_{zz} - R^2 m_b\right]\dot{\psi}^2\sin 2\beta_3 + \frac{R}{2}m_b g\cos\beta_3 = Q_{\beta_3} \tag{4.19}$$

$$\left[\frac{R^2}{4}m_b + I_{yy}\right]\ddot{\beta}_4 - \frac{1}{2}\left[I_{xx} - I_{zz} - R^2 m_b\right]\dot{\psi}^2\sin 2\beta_4 + \frac{R}{2}m_b g\cos\beta_4 = Q_{\beta_4} \tag{4.20}$$

The system is broken down into coupled first-order equations and then solved using numerical integration techniques.

4.1 Model Validation

To validate the method, the model needs to converge to the steady state values predicted by the static analysis done in [6]. Since the model contains four blades each blade must be represented by its own equations of motion. In state-space this equates to a total of ten

coupled first order differential equations. The parameters shown in table 4.1 and appendix C.1 are utilized to simulate the results of the dynamic model and show that convergence is attained.

Table 4.1: Dynamic simulation parameters

Parameter	Value	Description
θ_0	0.0698	Blade pitch (rad)
ρ	0.000801352	Air density (slugs/ft^3)
m_b	$\frac{3I_1}{R^2}$	Mass of one blade (slugs)
t_h	$.12c$	Thickness of airfoil
Izz	$\frac{m_b}{12(c^2+R^2)}$	Moment of inertia of blade around z
I_{xx}	$\frac{mblade}{12(t_h^2+c^2)}$	Moment of inertia of blade around x
I_{yy}	$\frac{mblade}{12(t_h^2+R^2)}$	Moment of inertia of blade around y

Initially, the steady state rotational speed of the dynamic model versus the prediction made using [6] is compared. The dynamic model and the steady-state model converge to a similar rotational speed with approximately 1% difference depicted in Fig.4.3 . The discrepancy of the two models can possibly be attributed to approximations made by [6] that were removed in the dynamic model. The approximations that were removed include the small angle approximation and the Fourier series approximation of cyclic blade flapping.

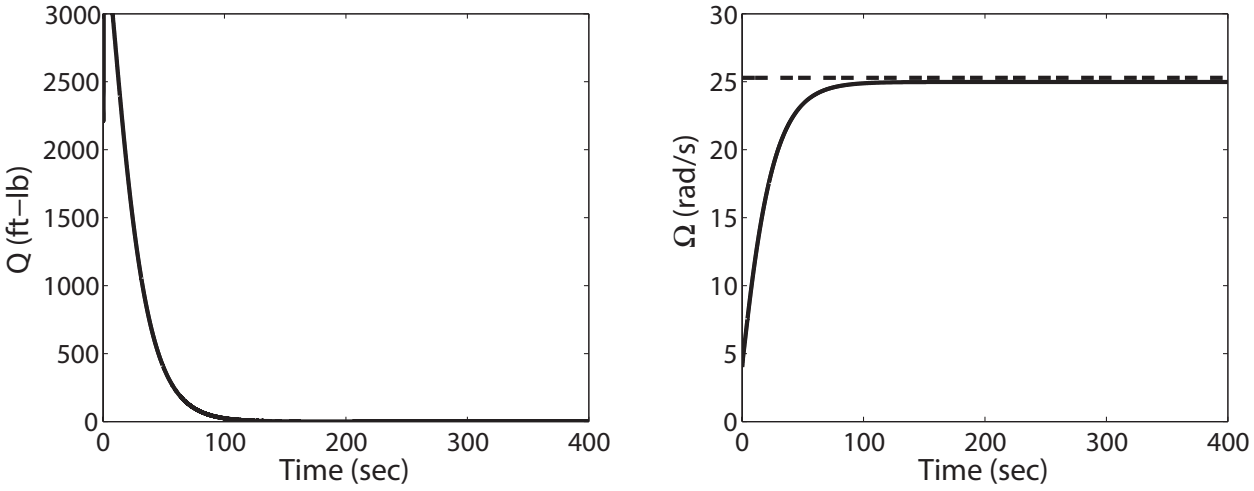

(a) (b)

Figure 4.3: (a) Dynamic Torque (b) Rotational Speed

Also note that the torque Fig.4.3a approaches zero as the system approaches steady-state, which is consistent with [6]. The torque Q_e at steady-autorotation should be zero because the aerodynamic forces causing positive and negative torque balance out where negative torque is due to parasitic drag. In section 5 the effect on torque from adding a generator load is examined.

The thrust converges to a value predicted from [6] shown in Fig.4.3b. The total steady-state thrust is not uniform because each blade has it's own harmonic thrust that cancel out as the system reaches steady state. The different harmonic thrust variations can be seen as one blade rotates through $0 - 2\pi$ in Fig.4.4d. A closer in-depth analysis shows that the total thrust has a harmonic of its own. This is of course insignificant at steady state conditions but may be important at unsteady conditions do the introduction of lateral forces.

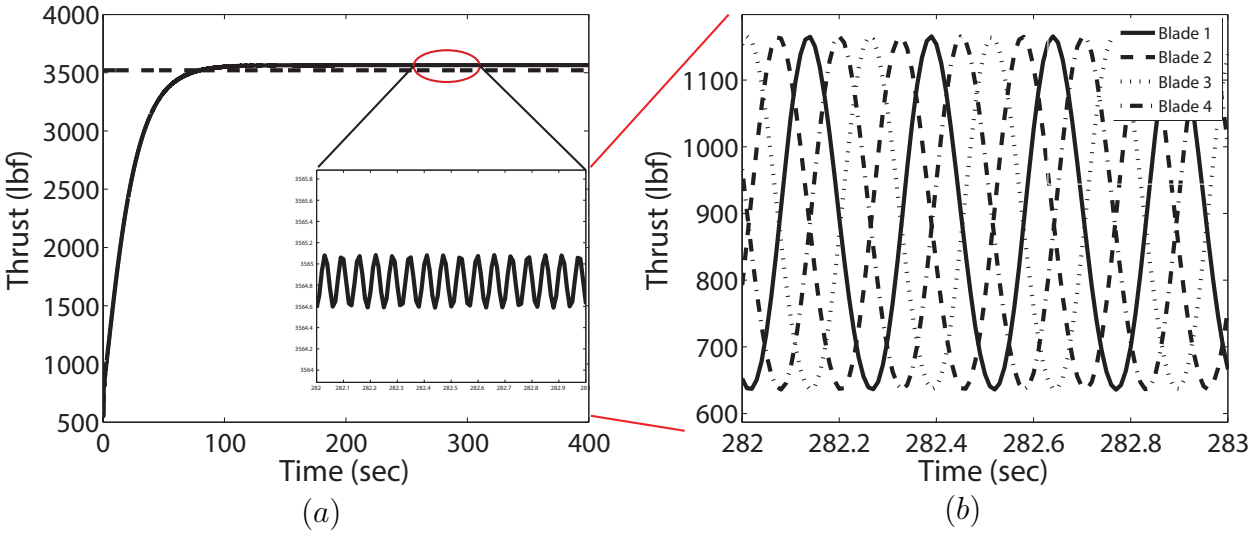

Figure 4.4: (a) Total Thrust (b) Individual Blade Thrusts

The steady-state flapping angle stays between $0.5 - 1.5$ degrees, which further supports the small angle approximation made in [6]. At steady state, the dynamic model shows cyclic flapping achieving a fixed frequency and amplitude as shown in Fig.4.5.

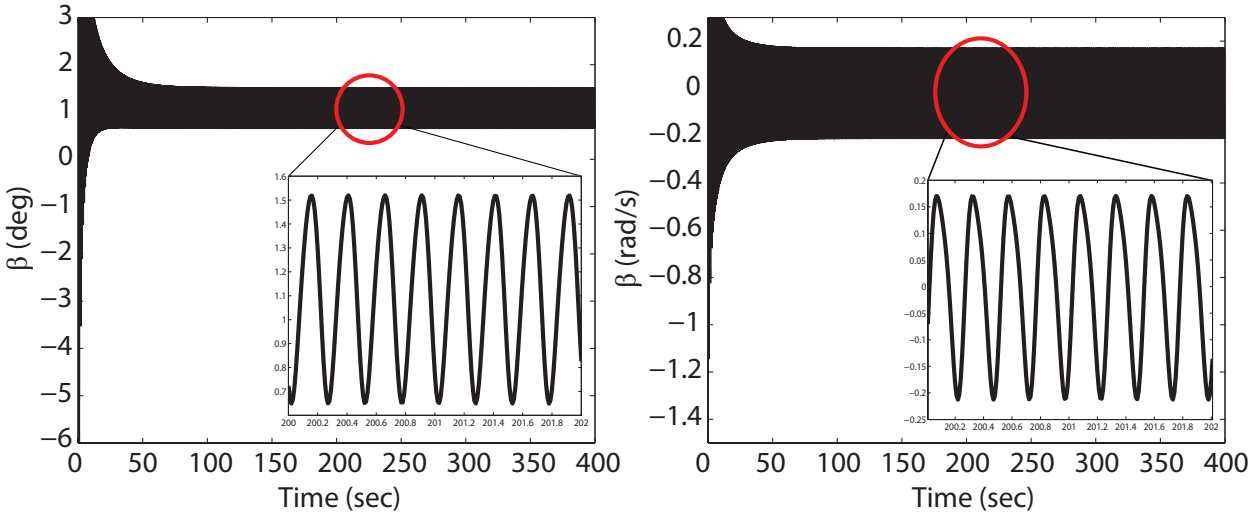

Figure 4.5: (a) Blade Flapping Angle (b) Blade Flapping Angular Velocity

From analyzing the motion of blade flapping, two main frequencies were found confirming

the original assumption made in [6], Fig.4.6. The first harmonic is approximately around 4 Hz and the second harmonic around 8 Hz. This relates to multiples of the rotational speed divided by 2π or the first and second natural frequencies of the system. Although two frequencies exit the second harmonic is significantly smaller and can potentially be neglected.

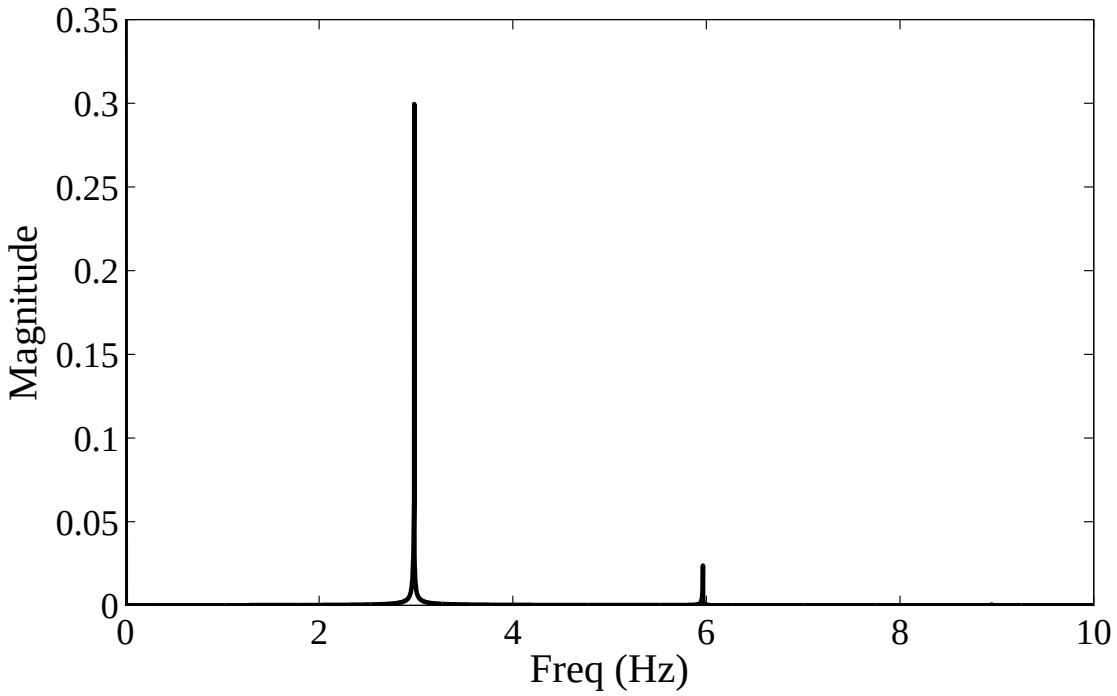

Figure 4.6: (a) Frequency of flapping angle (b) Frequency of flapping angular velocity

Going further an analysis of the autogyro in a changing wind field is simulated. At 300 seconds after the system has reached steady-state the wind velocity is dropped from 70 m/s to 60 m/s. The results are shown in Fig.4.7. The dashed lines represent the steady-state solutions from the model developed in section 3. The results show that the system does not experience any adverse affects but merely approaches steady-state at a lower rotational speed and thrust. The rotational torque Q_e becomes negative at the transition time and slowly approaches $Q_e = 0$ as predicted from the steady autorotation models.

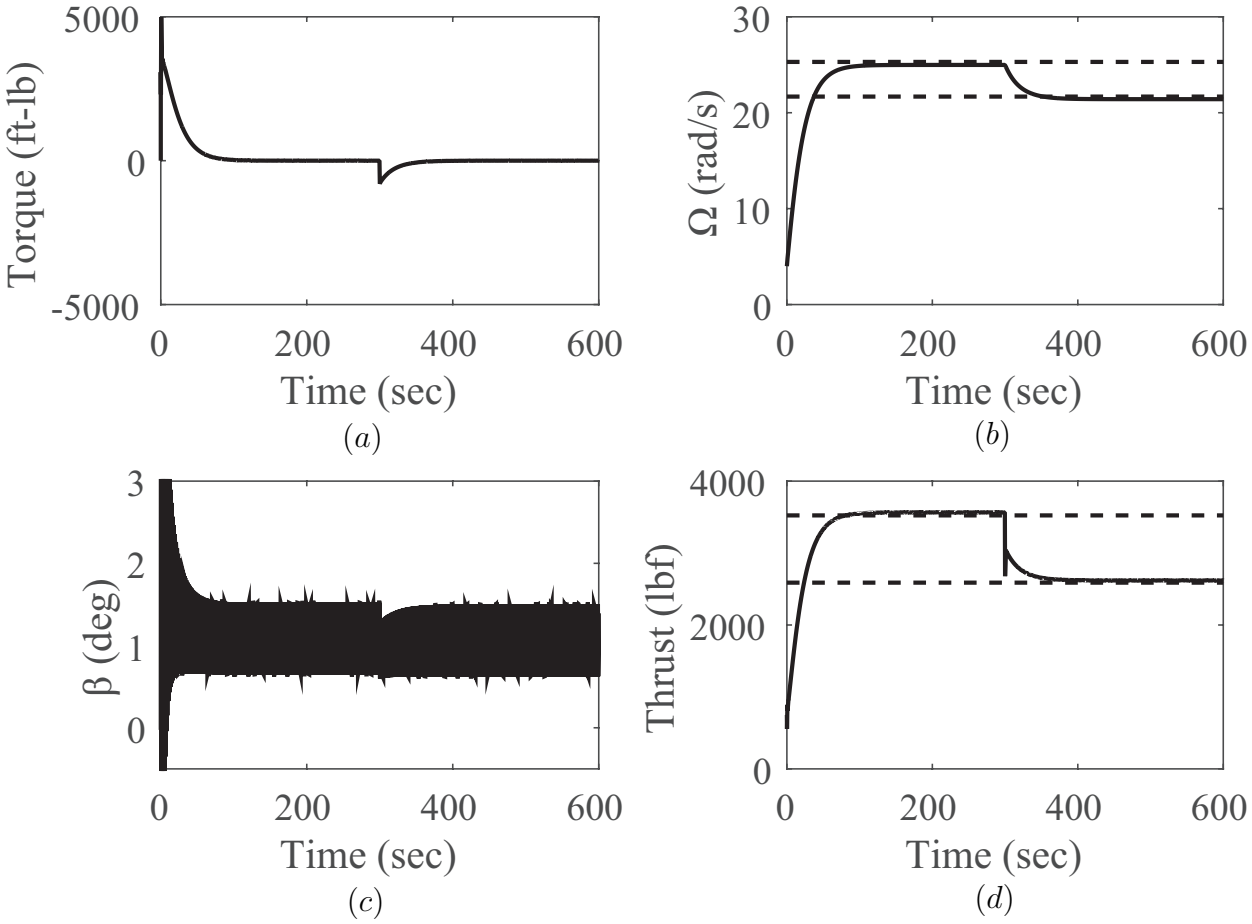

Figure 4.7: (a) Torque Q_e (b) Rotational Speed (c) Flapping of blade 1 (d) Thrust

The difficulty of using the model in [6] is the requirement of knowing the equilibria μ or tip-speed ratio. This ratio should naturally form from the initial wind velocity V and torque Q_e. To grasp the general operating condition this system would be experiencing, a range of wind velocities were run through the dynamic model to review the possible steady-state equilibria. The results are presented in Fig.4.8a and is found that for most wind velocities the tip-speed lies around $\mu = .11$. This implies that although the lower tip-speeds may be possible operating points, they may not necessarily be stable equilibria. Similarly, the thrust of blade 1 is examined as the wind velocity and torque are changed, Fig.4.8b. The results show the variation of thrust the blade experiences as the blade flaps. With higher wind

speeds the thrust increases but experiences much higher variations. As torque increases the thrust decreases as expected.

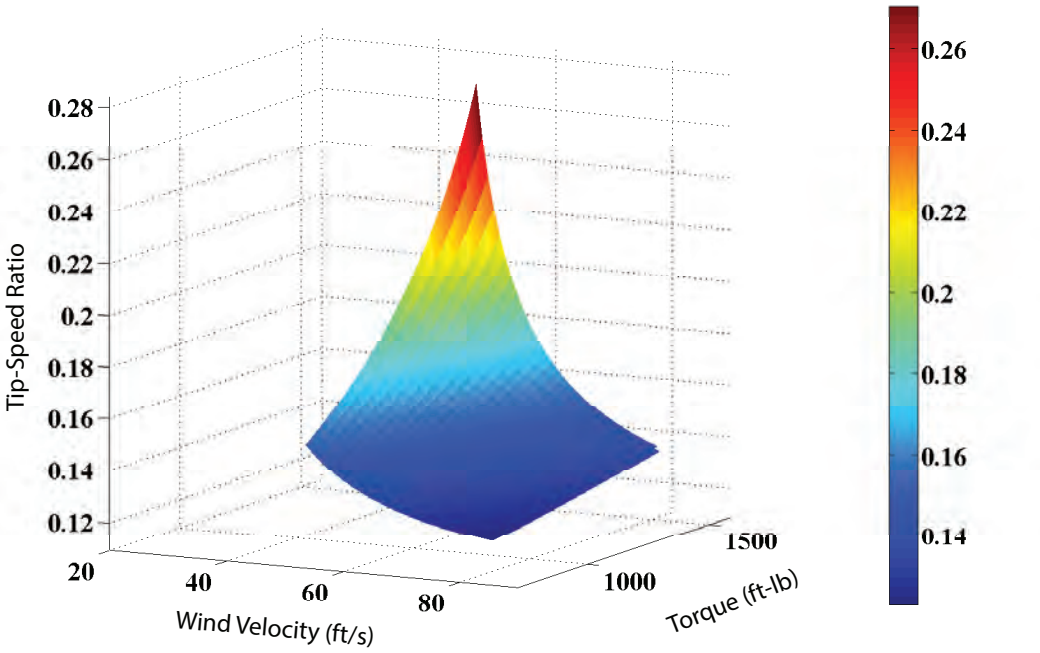

(a)

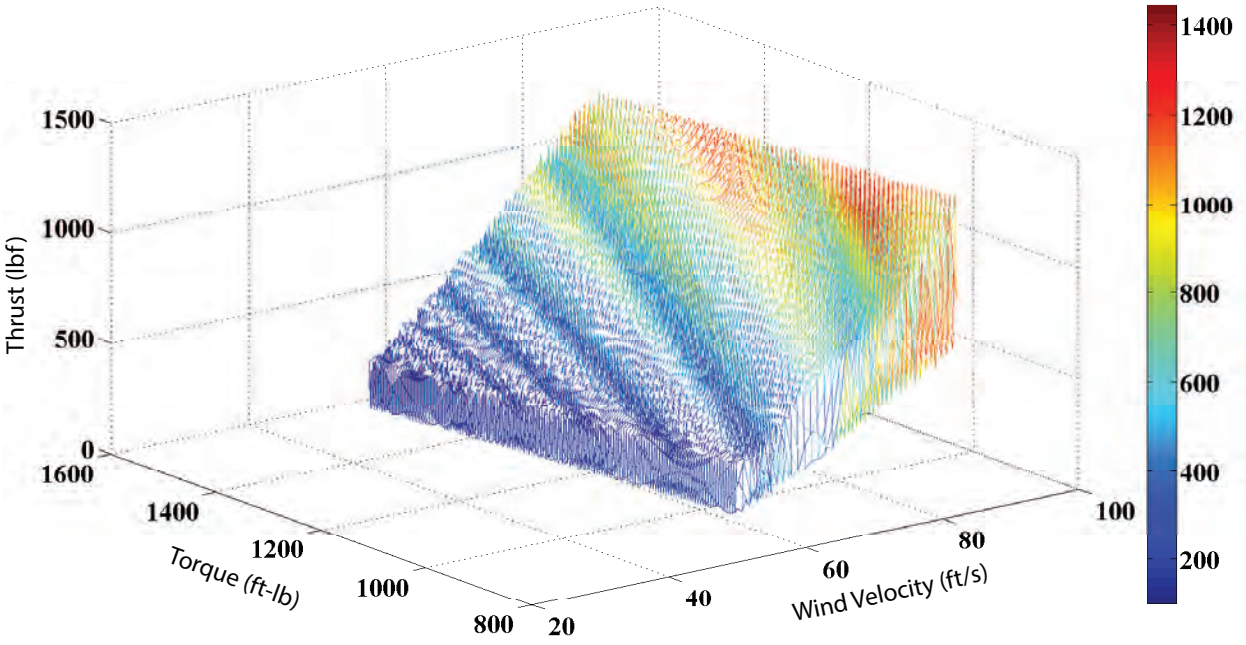

(b)

Figure 4.8: (a) Tip-Speed vs Wind Velocity and Torque (b) Thrust of blade 1 vs Wind Velocity and Torque

CHAPTER 5: ENERGY HARVESTING

The purpose of this research is to determine the feasibility of using an autogyro for energy extraction while maintaining sufficient lift. When a generator torque is introduced into a freely rotating autogyro a clear slowdown of the rotor rotational speed should occur. This slowdown should cause blade flapping angles to increase because of a lower centripetal acceleration.

Using the steady-autorotation model developed in section 3 and the dynamic model developed in section 4, the predicted behavior of the system under a generator load is compared. The application of a generator load is modeled as a parasitic torque thus a torque is subtracted from the RHS of Eq.4.9. Due to how the the method in [6] is developed the process of adding a parasitic torque is more complex. This is because the torque is taken as 0 and the equation is used to back-calculate the inflow ratio. That implies the addition of the torque will be a "correction" to the inflow Eq.3.10. This results in the difficulty of having to solve Ω and λ simultaneously. The problem is approached through numerical iteration, described in section 3, and the final results are presented in Fig.5.1.

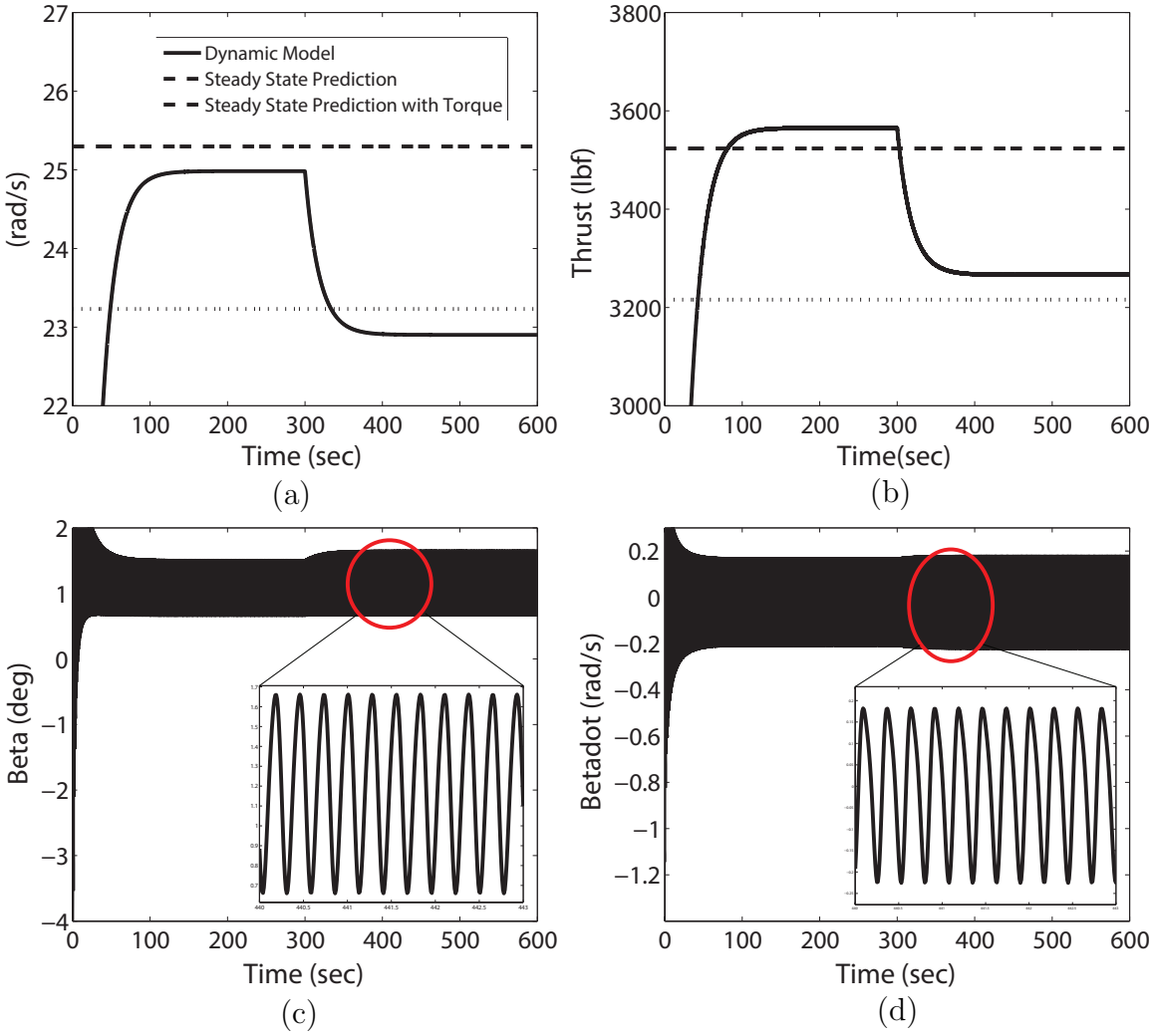

Figure 5.1: (a) Rotational Speed, (b) Thrust, (c) Flapping angle (d) Flapping angular velocity

For the first $<$ 300 seconds the autogyro is simulated with zero torque and allowed to reach steady-state at which point a 500 ft-lb torque is applied. As intuition predicted, the thrust and speed decrease when a torque is applied. From Fig.5.1, both models clearly have agreement on the rotational speed and thrust. The effect of applying a torque has minimal effect on the transient behavior because of the high inertia of the system. Therefore, chaotic behaviors are effectively nullified. Since both models show good agreement, the steady-

autorotation model in [6] is used to analyze the overall lift C_{L_T}, drag C_{D_R}, and required wind speed at 0 ft/lb and 500 ft/lb torques. From Fig.5.2c, the minimum wind velocity required at the operating angle of $\alpha = 30°$ with a weight of 3000 lbf is 20 m/s, where the expected wind speed at an altitude of 7 km is 21 m/s.

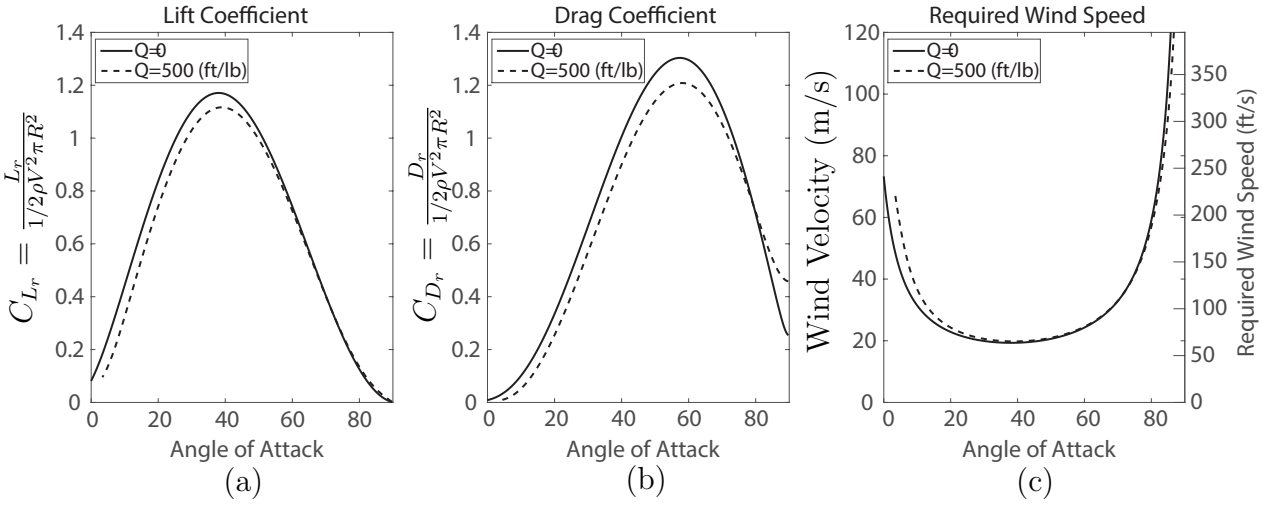

Figure 5.2: (a) Lift Coefficient (b) Drag Coefficient (c) Wind velocity required to maintain level flight

It's possible to surmise from Fig.5.1 that a craft of about 3250 lbf and below is required to maintain level flight and extract energy with the conditions and parameters imposed from Table 4.1. Since the blade weights are ~ 2 lbf there is easily enough room to add a generator to the system and still maintain flight. As predicted, Fig.5.1c shows the blade flapping increasing due to the slower rotational speed and thus lower centrifugal force. Finally, the overall thrust variation along the path of the blade is analyzed before and after the generator torque is applied, Fig.5.3. A slight shift in thrust occurs from the reverse half towards the forward half as a result of the slowdown of the rotational speed. As explained in section 3, the faster the rotor spins the less significant forward wind velocity becomes, Fig.2.9.

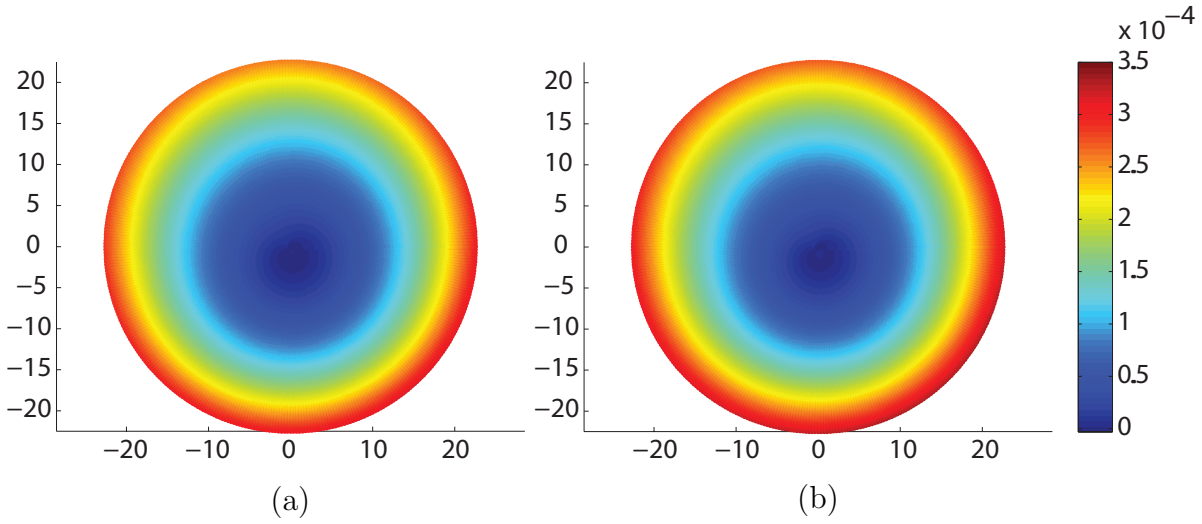

Figure 5.3: Thrust Coefficient: (a) No generator torque (b) 500 ft-lb generator torque

Conditions needed to maintain flight and extract energy for a range of torques is determined. The analysis utilized the system described in [6] with the system parameters presented in Table 3.1; the results are shown in Fig.5.4. Around 500 ft-lb the system would be extracting approximately $15kW$ of power. Initially, this seems low but persistent winds at high altitudes may allow for higher overall power generation. Further analysis and experimentation is required to understand the outcome.

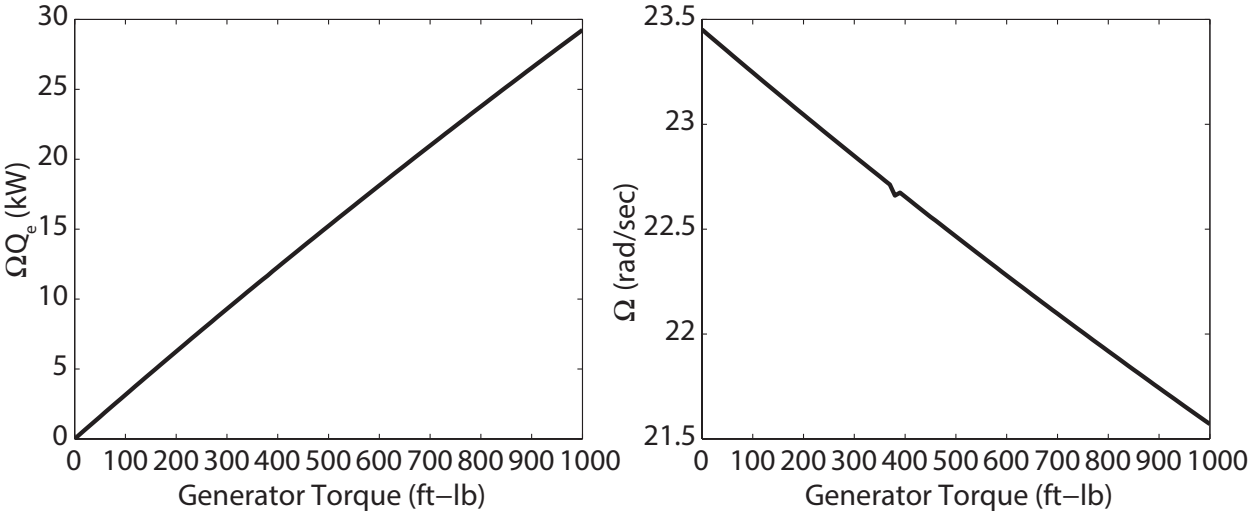

Figure 5.4: (a) Power extracted, (b) Angular rotation Ω at applied torque while maintaining sufficient lift

By analyzing a range of wind velocities V and generator torques (Q_e), an optimal power generation region can be determined. Fig.5.5 shows the ideal values of V and Q_e for generating the maximum amount of power. To account for the probability distributions of V at an attitude of 7 km a Weibull distribution is used. The Weibull distribution takes the form

$$P(V) = \left(\frac{k}{c}\right)\left(\frac{v}{c}\right)^{(k-1)} e^{-\left(\frac{v}{c}\right)^k} \tag{5.1}$$

where $k = 3$ and $V = 70$. The potential power output is then the steady-state predicted power output multiplied by the probability distribution. The simulation weight of the autogyro is 3000 lbf, therefore the predicted lift must be ≥ 3000. Thus any point producing lift $T\cos\alpha < 3000$, is set to 0 as this is not a potential operating point. Due to the Weibull distribution, 70 ft/s is the most probable wind speed, therefore the power generation will be maximal around this region. From Fig.5.5, a breaking torque 1200 ft/lb can be applied, however, a decrease in wind speed will cause the system to move to the region of lift lower than it's weight. Therefore, breaking torques ranging between 400-800 ft/lb are more conservative

and safer torques to apply as it leaves more room for wind speed variations.

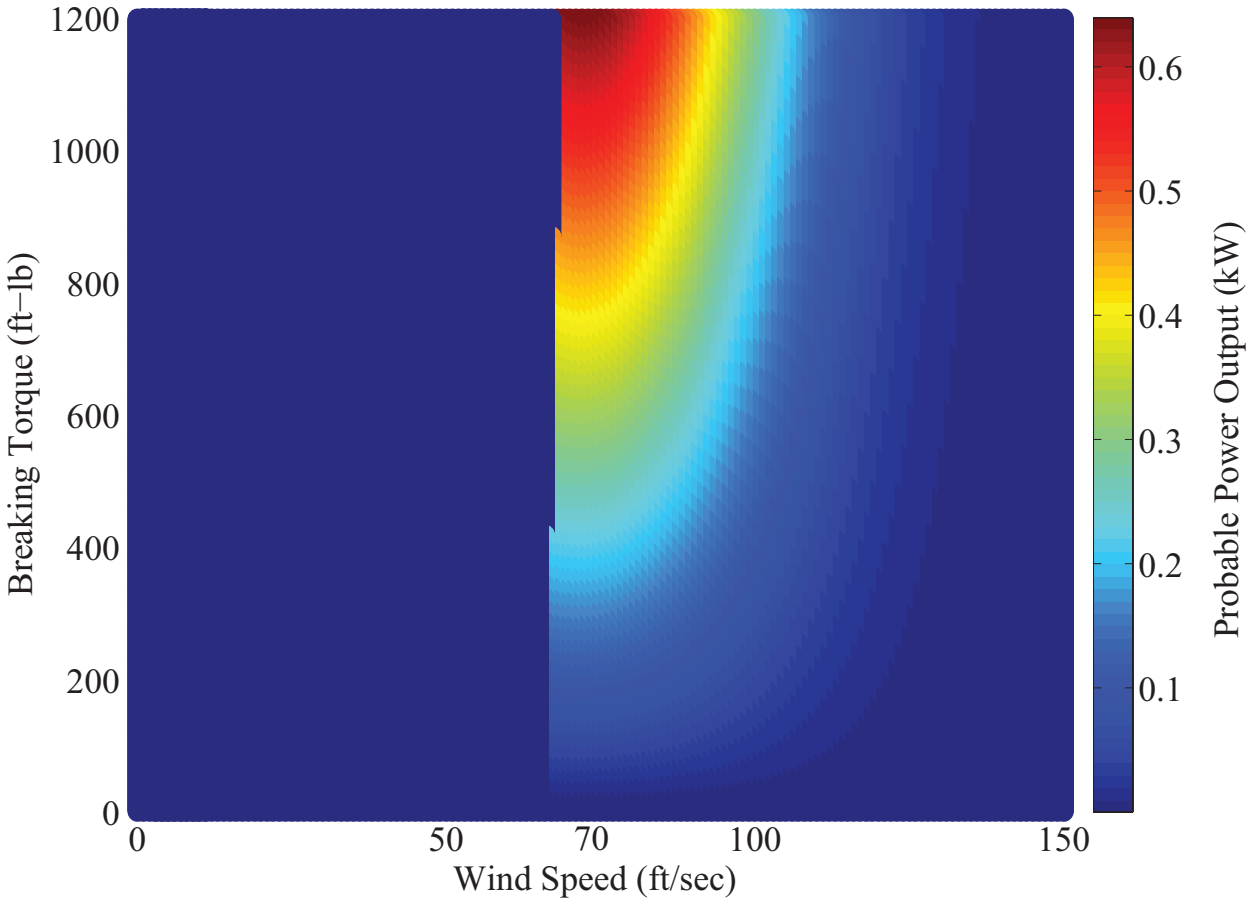

Figure 5.5: Probable power extraction at velocity V and torque Q

CHAPTER 6: OPTIMIZATION

To get a sense of the optimal operating height of an autogyro with an attached tether, a statics problem is solved. The goal is to determine the thrust (T) and angle of attack (α) that will provide the highest energy extraction while maintaining sufficient lift to hold up its own weight plus the weight of the tether. This will yield an optimal equilibrium point $(x*, y*)$ of the autogyro. For simplicity, only a 2-D case is considered, Fig.6.1(a).

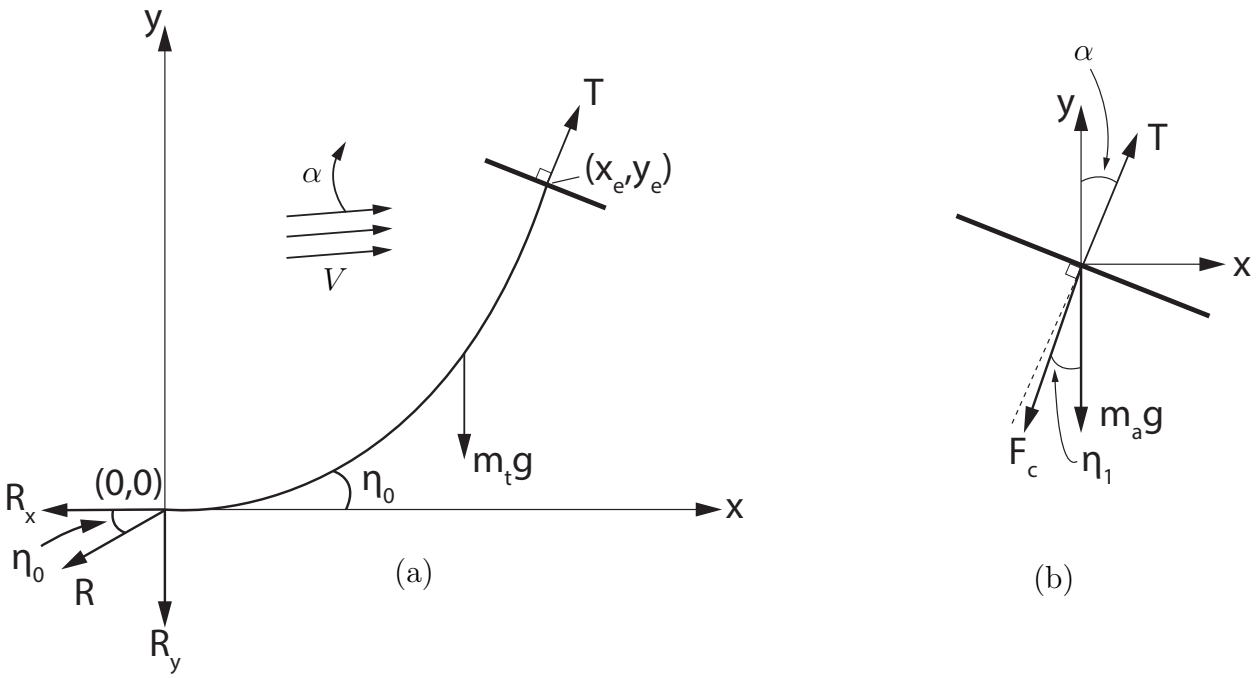

Figure 6.1: Tethered Autogyro

The shape of the tether is approximated as a catenary. The catenary shape is modeled as a hyperbolic function represented by

$$y_e = b\left[\cosh\left(\frac{x_e - q}{b}\right) - \cosh\left(\frac{q}{b}\right)\right] \tag{6.1}$$

where q and a define the shape of the tether [13]. Note that the tension is tangential at any point on the tether and not necessarily uniform, therefore, from [13] the following relations are used

$$\begin{aligned} l_t &= b\left(\sinh\left(\frac{y_e - q}{b}\right) - \sinh\left(\frac{-q}{b}\right)\right) \\ \tan\eta_0 &= \sinh\left(\frac{-q}{b}\right) = \frac{Ry}{Rx} \\ \tan\eta_l &= \sinh\left(\frac{x_e - q}{b}\right) = \frac{F_{c_y}}{F_{c_x}} \end{aligned} \tag{6.2}$$

where l_t is the length of the tether and x_e is the x-position of the free endpoint of the tether.

First, the system static equations are setup. Considering only the autogyro in Fig.6.1(b), the forces are summed in the x and y directions and equated to zero.

$$\begin{aligned} 0 &= T\sin\alpha - F_c\sin\eta_l \\ 0 &= T\cos\alpha - F_c\cos\eta_l - m_a g \end{aligned} \tag{6.3}$$

where F_c is the tension at the top of the tether and eta_1 is the angle made by the tether with the vertical. Similarly, the static equations for the entire system are

$$\begin{aligned} 0 &= T\sin\alpha - R\cos\eta_0 \\ 0 &= T\cos\alpha - R\sin\eta_0 - m_t g - m_a g \end{aligned} \tag{6.4}$$

where R is the tension at the bottom of the tether and eta_0 is the angle made by the tether with the horizontal. From [6], given tip-speeds have unique solutions for thrust T and angle-of-attack α. This implies that using equations 6.3 and 6.4 the tensions F_c and R and the

angles η_l and η_0 can be found. From substitution the expressions for η_l and η_0 are

$$\begin{aligned} \tan\eta_0 &= \frac{T\cos\alpha - (m_a + m_t)g}{T\sin\alpha} \\ \tan\eta_l &= \frac{T\cos\alpha - m_a g}{T\sin\alpha} \end{aligned} \tag{6.5}$$

where m_a and m_t are the mass of the autogyro and tether, respectively. Using the expressions in 6.2 and F_c, R, η_l, and η_0 the expressions for the constants q and b are

$$b = \frac{l_t}{\tan\eta_l - \tan\eta_0}, \qquad q = b\,\mathrm{arcsinh}\,(-\tan\eta_0) \tag{6.6}$$

where l_t is the length of the tether. Finally, the equilibrium point x_e can be extracted with

$$x_e = b\,\mathrm{arcsinh}\,(\tan\eta_l) + q \tag{6.7}$$

Using the calculated constants, the equilibrium point x_e, and Eq.6.1 the final equilibrium position (x_e, y_e) of the autogyro can be calculated.

6.1 Simulation

With the developed method, a range of tip-speeds, torques, and wind velocities were analyzed to understand the conditions required for energy extraction. For the simulation, the working altitude of the autogyro is set to 7 km or $\sim$ 23000 ft with a tether length l_t of 25000 ft. The tether is made of 11 AWG wires 2.3 mm in diameter with a Kevlar K-49 layer that has a thickness of 6 mm. This gives a tether weight of 86 lb/km or a total weight of $\sim$ 655 lbf for a 7 km tether. All other parameters used are listed in appendix C.1 and table 4.1 with the exception of the air density, which at an altitude of 7 km is $\rho = 0.0012408\ slug/ft^3$.

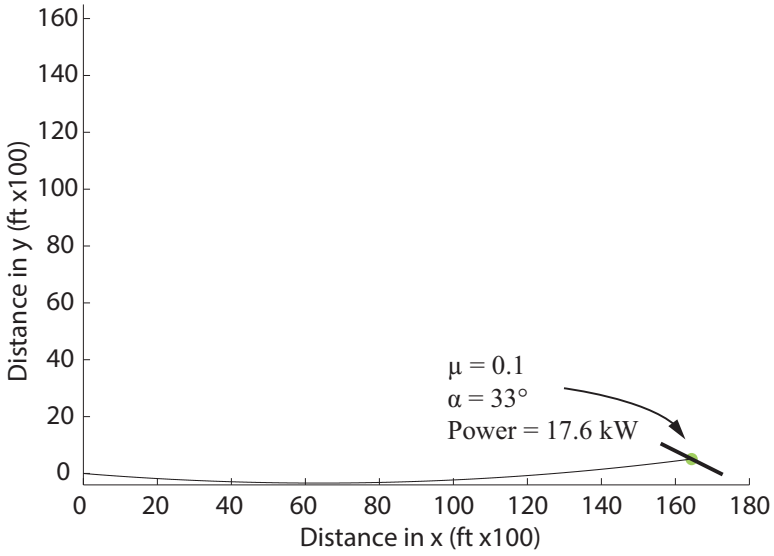

Figure 6.2: Tethered Autogyro (rotor disk size exaggerated for clarity of angle of attack)

The initial simulation using an autogyro weight of 3000 lbf shows extremely shallow angles with very high tether tension ranging from 3000-3600 lbf, Fig.6.2. Since a uniform wind distribution is used at all heights, this shallow angle is unrealistic because the autogyro would not be experiencing the same high wind velocities at low altitudes. Therefore, the autogyro must maintain sufficient height to take advantage of the high wind fields. It stands to reason that a multi-rotor craft similar to a quad-rotor would be the next logical step because not only do multi-rotor systems provide more lift there are inherent backups if there is a failure of a rotor. Therefore, picking a quadrotor system the weight each rotor would be required to lift is reduced by a quarter to 750 lbf.

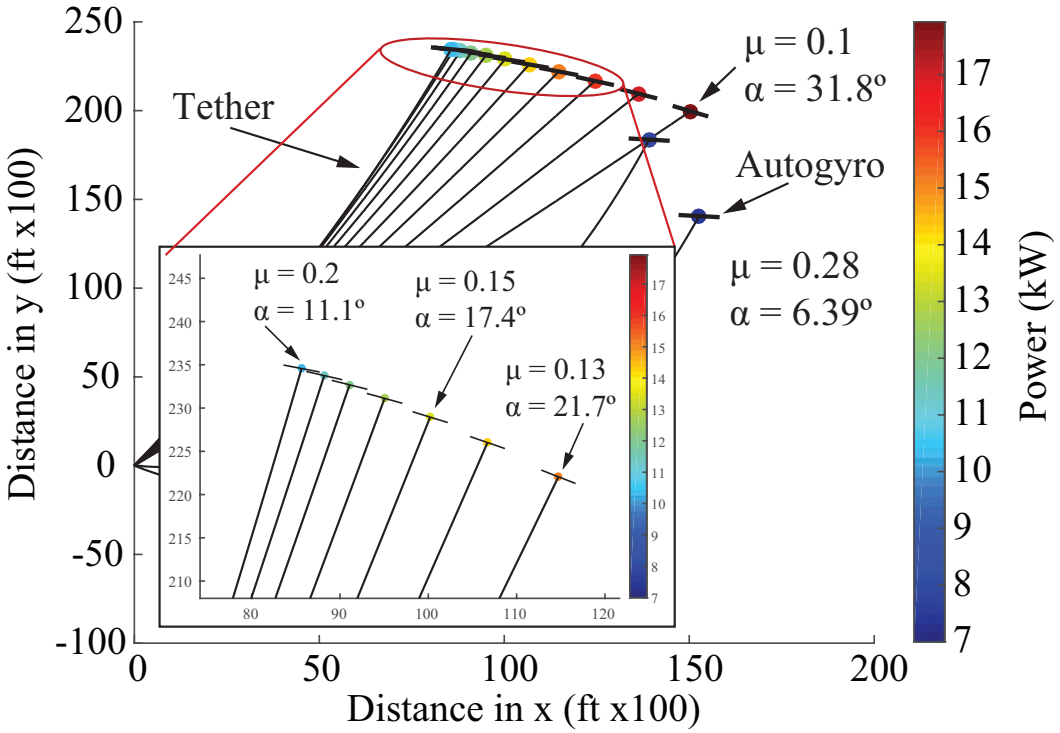

(a)

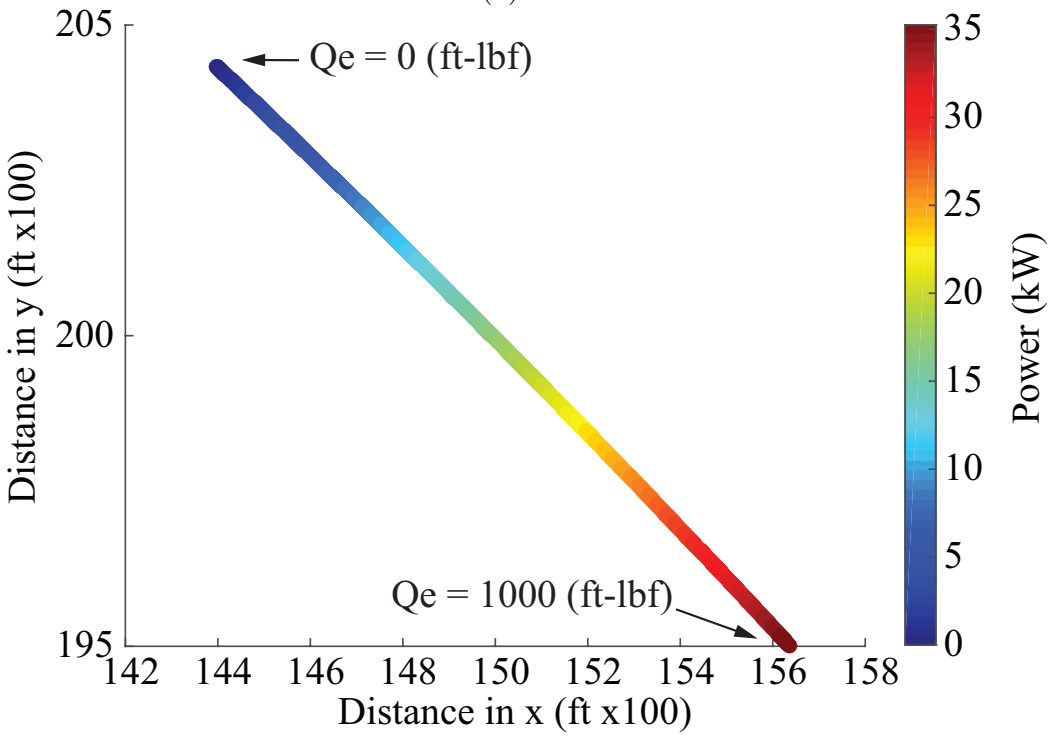

(b)

Figure 6.3: Tethered Autogyro: (a) Autogyro position at different rotational speeds with 500 ft-lb torque (b) Power with generator torque varied from 0-1000 ft-lb

With the reduction in weight an interesting phenomenon occurs for equilibrium points in Fig.6.3a. As the tip-speed is decreased the autogyro moves upward until hitting a critical point around $\mu = .2$ where the autogyro again starts to settle to a lower altitude. Fig.6.3b shows the max power generated as torque is varied from 0 to 1000 ft-lb. As generator load is increased the equilibrium point drops approximately 1000 ft but still maintains sufficient lift. From this work it is possible to conclude that collecting energy via autorotation is theoretically feasible and merits further research and experimental study.

CHAPTER 7: CONCLUSION

This thesis shows that persistent and pervasive winds at high-altitudes provides motivation for looking into self-levitating energy extraction devices. Autorotation was shown to be a possible means of high-altitude wind energy extraction. Initially, a review of the current steady-state model of autorotation was presented in [6]. After proving the model was developed correctly and to show the need for flapping, the thrust coefficient C_T was plotted as a blade rotates from $0-2\pi$ in Fig.3.6. To fill in the gaps of the steady-state model, specifically to understand the effect of a disturbance, a dynamic model was developed. In doing so the necessity, to know the equilibrium tip-speed ratio μ beforehand was removed. The model was validated by comparing the steady-state values of the dynamic model to the predicted values using the model in [6]. After verifying the dynamic model, a generator torque was introduced to understand how the system will react. The system was found to remain stable and reach a new equilibrium point. Finally, an optimal angle-of-attack for maximizing energy extraction while maintaining sufficient lift was presented.

7.1 Further Research

The dynamic model presented in this thesis uses an inertial frame on the fixed point of rotation and thus does not consider a spatially translating autogyro. A way to alleviate this issue is by using the ground as the inertial frame of reference. By using a new position vector from the inertial frame to the center of rotation plus the position vector to the center of mass of each blade from the center of rotation, the new translational kinetic energy of the system can be derived, Fig.7.1. The addition of this motion requires adjustments to the non-conservative aerodynamic forces because the relative wind-velocities a blade will experience

will depend on position. For a four blade system the coupled equations of motion will jump from **10** first-order coupled differential equations to **16** coupled differential equations.

Other enhancements to the model include eliminating the approximation of the wing as a cuboid and considering real airfoils with known inertias and better lift coefficients. Also, incorporating the hub into the dynamics is an important aspect to study as it affects the blade moments. Even though explicitly stated in [6] that the hub radius effects are negligible, a thorough review must be done in order to be certain. Since the blades that are considered in this thesis are relatively long, other aspects such as dynamic inflow as described in [52] and blade bending and torsion that affect flight stability should be considered [51].

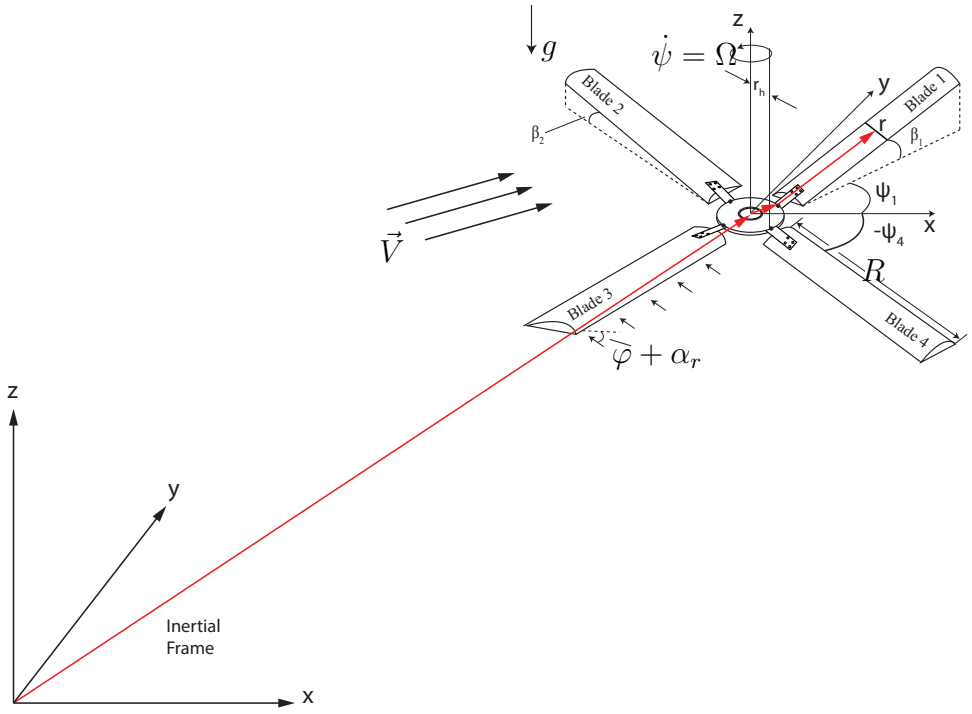

Figure 7.1: Position vector from Earth fixed inertial frame

A big concern with using an autogyro is the question of sufficient lift. A relatively simple way to alleviate this issue is by using a multi-rotor configuration such as a quadrotor, Fig.7.2.

Extensive literature on multi-rotor dynamics and control can be leveraged. The benefit of using a quadrotor setup with flapping blades is the reduction of blade size. The smaller configuration will allow for better maneuverability and agility in the presence of variable wind fields. A generator on a quadrotor setup could serve a dual purpose of collecting energy and controlling rotational speeds. While a normal powered quadrotor uses motors to achieve uniform rotational speeds, an autogyro in a crosswind can use a generator to achieve the same effect for rotors experiencing different wind speeds by controlling the generator load. In the event of rotor failure the autogyro can still take advantage of autorotation to land safely, which is an important aspect for flight safety.

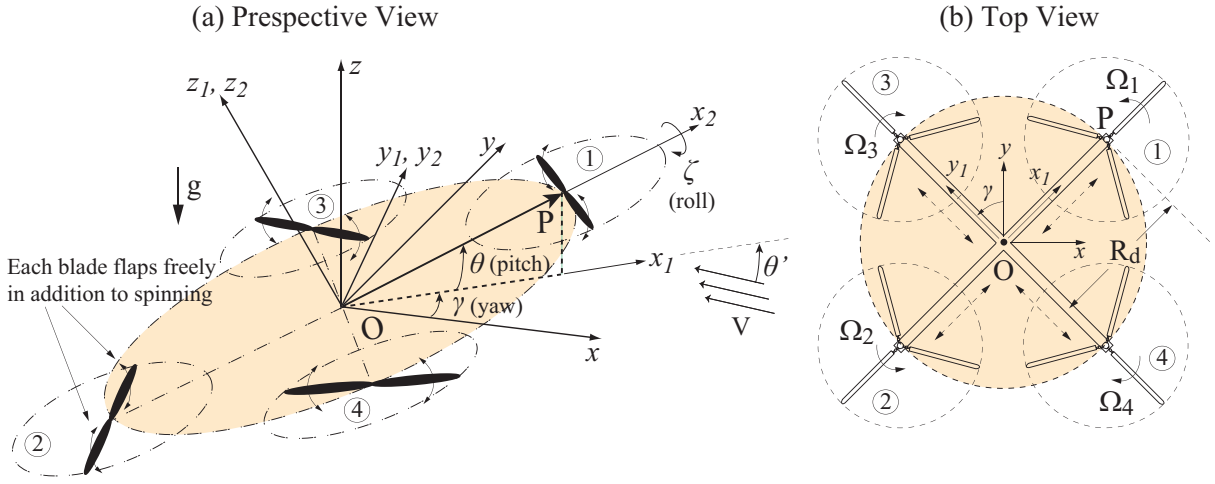

Figure 7.2: Autogyro quadrotor configuration

The difficult aspect of using a quadrotor relies on deriving the necessary equations of motion. Although, dynamics of powered quadrotors have been thoroughly researched, incorporating the dynamics of blade flapping add significant levels of complexity. However, deriving complete and accurate dynamic models are the first steps to developing a control system. The complexity of this system makes control difficult and merits further research.

APPENDIX A: CUBOID

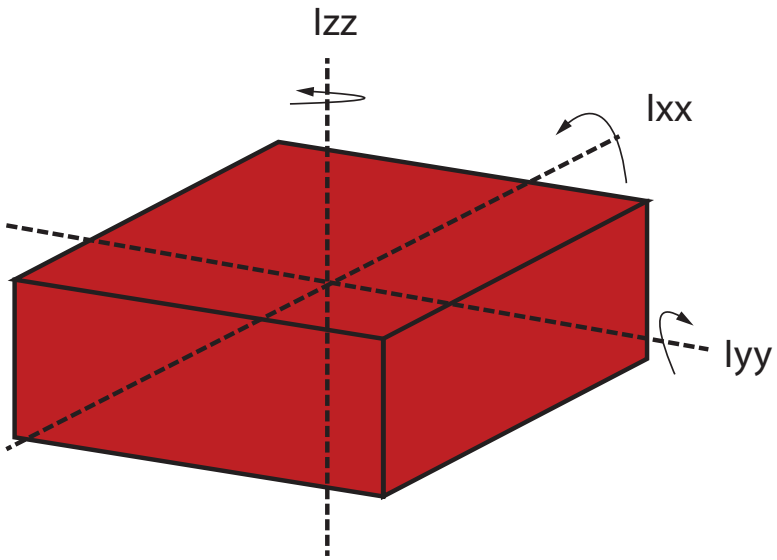

Figure A.1: Cuboid

$$Ixx = \frac{m}{12}\left(c^2 + th^2\right) \tag{A.1}$$

$$Iyy = \frac{m}{12}\left(th^2 + R^2\right) \tag{A.2}$$

$$Izz = \frac{m}{12}\left(c^2 + R^2\right) \tag{A.3}$$

APPENDIX B: FOURIER COEFFICEINTS

$$a_0 = \frac{1}{2}\gamma \left\{ \frac{1}{3}\lambda B^3 + 0.080\mu^3\lambda + \frac{1}{4}\theta_0 \left(B^4 + \mu^2 B^2 - \frac{1}{8}\mu^4 \right) + \frac{1}{5}\theta_1 \left(B^5 + \frac{5}{6}\mu^2 B^3 \right) + \frac{1}{8}\mu^2 b_2 B^2 \right\} - \frac{M_w}{I\Omega^2} \tag{B.1}$$

$$a_1 = \frac{2\mu}{B^4 - \frac{1}{2}\mu^2 B^2} \left\{ \lambda \left(B^2 - \frac{1}{4}\mu^2 \right) + \frac{4}{3}\theta_0 B^3 + 0.106\mu^3\theta_0 + \theta_1 B^4 - \frac{1}{3}b_2 B^3 \right\} \tag{B.2}$$

$$b_1 = \frac{4\mu B}{B^2 + \frac{1}{2}\mu^2} \left\{ \frac{1}{3}a_0 + \frac{0.035}{B^3}\mu^3 a_0 + \frac{1}{6}a_2 \right\} \tag{B.3}$$

$$a_2 = \frac{\gamma\mu^2}{144 + \gamma^2 B^8} \left\{ \lambda B \left(16 + \frac{7}{108}\gamma^2 B^8 \right) + \theta_0 B^2 \left(\frac{46}{3} + \frac{7}{144}\gamma^2 B^8 \right) + \theta_1 B^3 \left(12 + \frac{7}{180}\gamma^2 B^8 \right) \right\} \tag{B.4}$$

$$b_2 = \frac{-\gamma^2\mu^2}{144 + \gamma^2 B^8} \left\{ \frac{5}{9}\lambda B^5 + \frac{25}{36}\theta_0 B^6 + \frac{8}{15}\theta_1 B^7 \right\} \tag{B.5}$$

where

$$\gamma = \frac{c\rho a R^4}{I_1} \tag{B.6}$$

APPENDIX C: PARAMETERS

Table C.1: General Simulation Parameters

Parameter	Value	Description
V	70	Wind Velocity (ft/s)
W_d	3000	Total weight of autogyro (lbs.)
Q_e	0-1000	Generator Torque (lb.ft)
b	4	Number of blades
R	22.5	Blade radius (ft)
I_1	334	Inertia about flapping hinge slug.ft^2
c	1.833	Blade chord (ft)
K	0.5	Ratio of ν and ν_1
B	$\frac{R-\frac{1}{2}c}{R}$	Non-dimensional Constant
a	5.85	Lift curve slope
σ	$\frac{Bc}{\pi R}$	Rotor solidity
δ	0.0120	Mean airfoil drag coefficient
γ	$\frac{c\rho a R^4}{I}$	mass constant

APPENDIX D: COMPLETE GENERALIZED FORCES

Torque Forward Flow Region

$$
\begin{aligned}
Q_{\psi_1} = -1/24 \Big(\Big(& 6\dot{\psi}^2\mu^2 \sin(\psi)^2 + 8\dot{\psi}^2\mu \sin(\psi) + 3\dot{\psi}^2 \Big) R^4 \delta \cos(\beta) - \Big(3B^4 R^4 \dot{\beta}^2 - \Big(3B^4 \dot{\psi}\theta_0 \\
& -4 \Big(2\dot{\psi}\mu \cos(\psi) \sin(\beta) - \dot{\psi}\mu\theta_0 \sin(\psi) - 2\dot{\psi}\lambda \cos(\beta) \Big) B^3 \Big) R^4 \dot{\beta} \\
& -2 \Big(2 \Big(\dot{\psi}^2\mu \cos(\psi) \sin(\beta) - \dot{\psi}^2\lambda \cos(\beta) \Big) B^3\theta_0 - 3 \Big(\dot{\psi}^2\mu^2 \cos(\psi)^2 \sin(\beta)^2 \\
& -2\dot{\psi}^2\lambda\mu \cos(\beta) \cos(\psi) \sin(\beta) + \dot{\psi}^2\lambda^2 \cos(\beta)^2 - \Big(\dot{\psi}^2\mu^2 \cos(\psi) \sin(\beta) \\
& -\dot{\psi}^2\lambda\mu \cos(\beta) \Big) \theta_0 \sin(\psi) \Big) B^2 \Big) R^4 \Big) a \cos(\beta) \Big) c\rho
\end{aligned} \tag{D.1}
$$

Torque Reverse Flow Region

$$
\begin{aligned}
Q_{\psi_2} = 1/12 \Big(& \dot{\psi}^2 R^4 \delta\mu^4 \cos(\beta) \sin(\psi)^4 - \Big(3R^4 \dot{\beta}^2 \mu^4 \sin(\psi)^4 + \Big(\dot{\psi}\mu^4\theta_0 \sin(\psi)^4 \\
& -8 \Big(\dot{\psi}\mu^4 \cos(\psi) \sin(\beta) - \dot{\psi}\lambda\mu^3 \cos(\beta) \Big) \sin(\psi)^3 \Big) R^4 \dot{\beta} - 2 \Big(\Big(\dot{\psi}^2\mu^4 \cos(\psi) \sin(\beta) \\
& -\dot{\psi}^2\lambda\mu^3 \cos(\beta) \Big) \theta_0 \sin(\psi)^3 - 3 \Big(\dot{\psi}^2\mu^4 \cos(\psi)^2 \sin(\beta)^2 - 2\dot{\psi}^2\lambda\mu^3 \cos(\beta) \cos(\psi) \sin(\beta) \\
& +\dot{\psi}^2\lambda^2\mu^2 \cos(\beta)^2 \Big) \sin(\psi)^2 \Big) R^4 \Big) a \cos(\beta) \Big) \rho
\end{aligned} \tag{D.2}
$$

Flapping Moment Forward Flow Region

$$
\begin{aligned}
Q_{\beta_1} = -1/24 \Big(& \Big(4B^3\dot{\psi}\mu \sin(\psi) + 3B^4\dot{\psi} \Big) R^4 \dot{\beta} - \Big(3B^4\dot{\psi}^2\theta_0 - 4 \Big(\dot{\psi}^2\mu \cos(\psi) \sin(\beta) \\
& -2\dot{\psi}^2\mu\theta_0 \sin(\psi) - \dot{\psi}^2\lambda \cos(\beta) \Big) B^3 + 6 \Big(\dot{\psi}^2\mu^2\theta_0 \sin(\psi)^2 - \Big(\dot{\psi}^2\mu^2 \cos(\psi) \sin(\beta) \\
& -\dot{\psi}^2\lambda\mu \cos(\beta) \Big) \sin(\psi) \Big) B^2 \Big) R^4 \Big) ac\rho \cos(\beta)
\end{aligned} \tag{D.3}
$$

Flapping Moment Reverse Flow Region

$$Q_{\beta_2} = -1/12 \left(\dot{\psi} R^4 \dot{\beta} \mu^4 \sin(\psi)^4 + \left(\dot{\psi}^2 \mu^4 \theta_0 \sin(\psi)^4 - 2 \left(\dot{\psi}^2 \mu^4 \cos(\psi) \sin(\beta) - \dot{\psi}^2 \lambda \mu^3 \cos(\beta) \right) \sin(\psi)^3 \right) R^4 \right) ac\rho \cos(\beta) \tag{D.4}$$

Thrust Forward Flow Region

$$T_1 = -1/12 \left(\left(3B^2 \dot{\psi} \mu \sin(\psi) + 2B^3 \dot{\psi} \right) R^3 \dot{\beta} - \left(2B^3 \dot{\psi}^2 \theta_0 - 3 \left(\dot{\psi}^2 \mu \cos(\psi) \sin(\beta) - 2\dot{\psi}^2 \mu \theta_0 \sin(\psi) - \dot{\psi}^2 \lambda \cos(\beta) \right) B^2 + 6 \left(\dot{\psi}^2 \mu^2 \theta_0 \sin(\psi)^2 - \left(\dot{\psi}^2 \mu^2 \cos(\psi) \sin(\beta) - \dot{\psi}^2 \lambda \mu \cos(\beta) \right) \sin(\psi) \right) B \right) R^3 \right) ac\rho \tag{D.5}$$

Thrust Reverse Flow Region

$$T_2 = 1/6 \left(\dot{\psi} R^3 \dot{\beta} \mu^3 \sin(\psi)^3 + \left(2\dot{\psi}^2 \mu^3 \theta_0 \sin(\psi)^3 - 3 \left(\dot{\psi}^2 \mu^3 \cos(\psi) \sin(\beta) - \dot{\psi}^2 \lambda \mu^2 \cos(\beta) \right) \sin(\psi)^2 \right) R^3 \right) ac\rho \tag{D.6}$$

LIST OF REFERENCES

[1] "Dynamic maps, gis data, and analysis tools." `http://www.nrel.gov/gis/wind.html`.

[2] "American wind energy association." `http://www.awea.org/`.

[3] R. V. M. F. Antonello Cherubini, Andrea Papini, "Airborne wind energy systems: A review of the technologies," *Renewable and Sustainable Energy Reviews*, pp. 1462–75, 2015.

[4] J. G. Leishman, "Development of the autogiro: A technical perspective," *Journal of Aircraft*, vol. 41, no. 4, pp. 765–781, 2004.

[5] G. A., "Review of information on induced flow of a lifting rotor. naca technical note," *National Advisory Committee for Aeronautics*, 1954.

[6] J. B. Wheatley, "An aerodynamic analysis of the autogiro rotor with a comparison between calculated and experimental results," *National Advisory Committee for Aeronautics, Report No. 487*, 1934.

[7] B. W. Roberts, D. H. Shepard, K. Caldeira, M. E. Cannon, D. G. Eccles, A. J. Grenier, and J. F. Freidin, "Harnessing high-altitude wind power," *IEEE Transactions on Energy Conversion*, vol. 22, pp. 136–144, 2007.

[8] C. L. Archer and K. Caldeira, "Global assessment of high-altitude wind power," *Energies*, vol. 2, pp. 307–319, 2009.

[9] D. Elliott, M. Schwartz, S. Haymes, D. Heimiller, G. Scott, M. Brower, E. Hale, and B. Phelps, *New Wind Energy Resource Potential Estimates for the United States*. National Renewable Energy Laboratory, NREL Report No. PR-5500-50439, 2011.

[10] M. Garcia-Sanz and C. H. Houpis, *Wind Energy Systems: Control Engineering Design*. CRC Press, 2012.

[11] T. Das, R. Mukherjee, and J. Cameron, "Optimal trajectory planning for hot-air balloons in linear wind fields," *AIAA Journal of Guidance, Control, and Dynamics*, vol. 26, no. 3, pp. 416–424, 2003.

[12] T. Das, R. Mukherjee, R. Sridhar, and A. Hellum, "Two dimensional modeling and simulation of a tethered airfoil system for harnessing wind energy," *Proceedings of the ASME Dynamic Systems and Control Conference, Arlington, VA*, 2011.

[13] S. Rimkus, T. Das, and R. Mukherjee, "Stability analysis of a tether-airfoil system," *American Control Conference, Washington DC*, 2013.

[14] B. H. Charnov, *From Autogiro to Gyroplane: The Amazing Survival of an Aviation Technology*. Praeger Publishers, Westport CT, 2003.

[15] "Gyrocopter vs helicopter." http://www.phenix.aero/PHE-1210.html, 2013.

[16] J. G. Leishman, *Principles of Helicopter Aerodynamics*. Cambridge University Press, 2000.

[17] H. Glauert, "A general theory of the autogyro," *Presented by the Director of Scientific Research Air Ministry, Reports and Memoranda No. 1111 (Ae. 285)*, 1926.

[18] A. Gessow and G. C. Myers Jr., *Aerodynamics of the Helicopter*. Macmillan Company, New York, 1952.

[19] J. B. Wheatley, "The aerodynamic analysis of the gyroplane rotating-wing system," *National Advisory Committee for Aeronautics, Technical Note No. 492*, 1934.

[20] J. B. Wheatley, "An analytical and experiental study of the effect of periodic blade twist on the thrust, torque, and flapping motion of an autogiro rotor," *National Advisory Committee for Aeronautics, Technical Note No. 591*, 1937.

[21] A. Gessow and A. D. Crim, "An extension of lifting rotor theory to cover operations at large angles of attack and high inflow conditions," *National Advisory Committee for Aeronautics, Technical Note No. 2665*, 1952.

[22] S. Rimkus and T. Das, "An application of the autogyro theory to airborne wind energy extraction," *ASME Dynamic Systems and Control Conference (DSCC), Palo Alto, CA*, October, 2013.

[23] "Roadmap 2050, a practical guide to a prosperous low-carbon europe," 2010.

[24] "20 percent wind energy by 2030: Increasing wind energy's contribution to u.s. electricity supply," *Energy Efficiency and Renewable Energy*, 2008.

[25] "Central intelligence agency." https://www.cia.gov/library/publications/ the-world-factbook/rankorder/2233rank.html.

[26] C. K. Marvel K, Kravitz B, "Geophysical limits to global wind power," *Nature Cloimate Change*, pp. 118–121, 2012.

[27] K. A. Miller LM, Gans F, "Jet stream wind power as a renewable energy resource; littler power, big impacts," *Earth System Dynamics*, pp. 201–212, 2011.

[28] "Sky windpower." `www.skywindpower.com`, 02 2016.

[29] P. Willams, "Optimal wind power extraction with a tethered kite," *AIAA Guidance, Navigation and Control Conference*, August 2006.

[30] P. Williams, B. Lansdorp, and W. Ockels, "Optimal cross-wind towing and power generation with tethered kites," *AIAA Journal of Guidance, Control and Dynamics*, vol. 31, no. 1, pp. 81–93, 2008.

[31] P. Williams, B. Lansdorp, and W. Ockels, "Nonlinear control and estimation of a tethered kite in changing wind conditions," *AIAA Journal of Guidance, Control and Dynamics*, vol. 31, no. 3, pp. 793–798, 2008.

[32] P. Williams, B. Lansdorp, and W. Ockels, "Modeling and control of a kite on a variable length flexible inelastic tether," *AIAA Modeling and Simulation Technologies Conference and Exhibit*, August 2007.

[33] B. M. K. N. D. N. Perković K, Silva P, "Harvesting high altitude wind enery for power production: the concept based on magnus' effect," *Appl Energy*, pp. 151–60, 2012.

[34] M. G, "Über die abweichungder geschosse, und über eine abfallende erscheinung bei rotierenden körpern," *Ann Phys*, pp. 1–29, 1853.

[35] L. P. M. D. Griffith S, Hardham C, "Faired tether for wind power generation systems." PCT patent application WO2009142762, 2009.

[36] M. D. H. C. Griffith S, Lynn P, "Bimodal kite system." PCT patent application US2009072092, 2009.

[37] H. C. Griffith S, Lynn P, "Wind power generation." PCT patent application US7847426B1, 2010.

[38] L. DV, "Developing a 600 kw airborne wind turbine. abstract submitted to the airborne wind energy conference," *TU Delft*, 2015.

[39] C. N. H. Lock, "Further development of autogyro theory - part i," *National Advisory Committee for Aeronautics, Reports and Memoranda No. 1127 (Ae. 299)*, 1927.

[40] C. N. H. Lock, "Further development of autogyro theory - part ii: A general treatment of the flapping motion," *National Advisory Committee for Aeronautics, Reports and Memoranda No. 1127 (Ae. 299)*, 1927.

[41] J. B. Wheatley, "Wind-tunnel tests of a 10-foot-diameter gyroplane rotor," *National Advisory Committee for Aeronautics, Technical Note No. 536*, 1936.

[42] F. B. Jr., "A study of the torque equilibrium of an autogiro rotor," *National Advisory Committee for Aeronautics. NACA Technical Report 623*, 1938.

[43] J. De la Cierva, "The development of the autogiro," *Journal of the Royal Aeronautical Society*, vol. 30, no. 181, pp. 8–29, 1926.

[44] J. De la Cierva, "A letter to raes with comments on the paper presented by h. glauert on 20 january 1927," *Journal of the Royal Aeronautical Society*, vol. 31, no. 198, pp. 505–506, 1927.

[45] J. De la Cierva, "The autogiro," *Journal of the Royal Aeronautical Society*, vol. 34, no. 239, pp. 902–921, 1930.

[46] J. De la Cierva, "New developments of the autogiro," *Journal of the Royal Aeronautical Society*, vol. 39, pp. 1125–1143, Dec. 1935.

[47] H. Wimperis, "The rotating wing in aircraft," 1926.

[48] F. Harris, "Early rotorcraft–the roots of our technology," *presentation*, March 1992.

[49] A. W. N. P.A. Hufton and F. Bigg, "General investigation into the characteristics of the c.30 autogiro," *Reports and Memoranda No. 1859*, March 1939.

[50] J. Wheatley, "Lift and drag characteristics and gliding performance of an autogiro as determined in flight," *NACA Report No. 434*, May 1932.

[51] J. Trchalik, *Aeroelastic modelling of gyroplane rotors*. PhD thesis, University of Glasgow, 2009.

[52] H. S. Murakami Y., "Dynamic inflow modelling for autorotating rotors," *The Aeronautical Journal*, January 2008.

[53] H. S. Thomson D.G., "Advances in understanding autogyro flight dynamics," *64th American Helicopter Society Annual Forum*, April 2008.

[54] S. S. Houston, "Analysis of rotorcraft flight dynamics in autorotation," *Journal of Guidance, Control, and Dynamics*, vol. 25, no. 1, pp. 33–39, 2002.

[55] C. A. Lopez and V. L. Wells, "Dynamics and stability of an autorotating rotor/wing unmanned aircraft," *Journal of Guidance, Control, and Dynamics*, vol. 27, no. 2, pp. 258–270, 2004.

[56] J. G. Leishman, *Principles of Helicopter Aerodynamics, Second Edition*. Cambridge University Press, 2006.